# VELOCITY MEASUREMENTS AHEAD OF A SEMI-INFINITE BODY IN MAGNETOHYDRODYNAMIC FLOW WITH ALIGNED FIELDS

Thesis by
Bruce Meno Lake

In Partial Fulfillment of the Requirements
For the Degree of
Doctor of Philosophy

California Institute of Technology
Pasadena, California
1969

(Submitted May 28, 1969)

## ACKNOWLEDGMENTS

I would like to express my sincere gratitude to Dr. Hans W. Liepmann for suggesting this problem and for his continued encouragement and guidance during the course of this research. I also wish to thank Dr. B. H. Suzuki and Dr. J. A. Shercliff for many helpful discussions.

Thanks are also due Mrs. Geraldine Krentler for the typing of the manuscript.

I gratefully acknowledge the Ford Foundation and the California Institute of Technology for their financial assistance and the Office of Naval Research for their support of the research program under contract No. N00014-67-A-0094-0001.

# ABSTRACT

Experiments are described in which velocities were measured ahead of a semi-infinite Rankine body moving parallel to a uniform magnetic field in a conducting fluid. The flow disturbance in front of the body is found to increase in length as $N^{\frac{1}{2}}$, where N is the interaction parameter. In most of the experiments this parameter was varied from 4 to about 50. Measurements made along the axis of symmetry in the flow show that there is a relatively short region of stagnant fluid directly ahead of the body. The major part of the disturbance is found to consist of a much longer region in which the flow undergoes transition from conditions in the freestream to conditions near the body. Velocity profiles across the flow in this region show that for increased N, at a fixed distance ahead of the body, the velocity defect increases and the disturbance becomes more confined radially. Although the radial gradients in the flow increase with N, they are found to be much smaller than would be expected in a flow containing thin current layers. A physical model of the flow which has currents and pressures consistent with these results is discussed.

## TABLE OF CONTENTS

# LIST OF SYMBOLS

| | |
|---|---|
| $B_o$ | uniform applied magnetic field |
| $\underline{B} = \underline{B}^*/B_o$ | dimensionless magnetic field |
| $c_p$ | specific heat at constant pressure |
| d | diameter of halfbody |
| h | heat transfer coefficient |
| H | Bernoulli function |
| $\underline{j} = \underline{j}^*/\sigma U B_o$ | dimensionless current density |
| k | thermal conductivity |
| $p = (p^* - p_1)/\rho U^2$ | dimensionless pressure |
| $p_1$ | static pressure at upstream infinity |
| q | rate of heat transfer |
| $\underline{q} = \underline{q}^*/U$ | dimensionless velocity |
| r, x | cylindrical coordinates transverse and parallel to free-stream direction, respectively |
| T | temperature |
| U | velocity of upstream infinity |
| u | dimensionless x-component of velocity relative to body (in Part I)<br>normalized dimensionless x-component of velocity perturbation produced by body relative to displacement flow (in all except Part I, see Part II) |
| v | dimensionless r-component of velocity |

## LIST OF SYMBOLS (cont'd.)

| | |
|---|---|
| $x_b$ | distance from body stagnation point measured in body diameters |
| X | calibration parameter (see Part II) |
| $\rho$ | density |
| $\sigma$ | electrical conductivity |
| $\nu$ | kinematic viscosity |
| $\mu$ | permeability |
| $\omega$ | vorticity |

Dimensionless Parameters:

| | |
|---|---|
| $\alpha = B_o/U\sqrt{\rho\mu}$ | Alfvén number |
| $C_D = D/\frac{1}{2}\rho U^2 \frac{\pi}{4} d^2$ | drag coefficient |
| $M = B_o d\sqrt{\sigma/\rho\nu}$ | Hartmann number |
| $N = \sigma B_o^2 d/\rho U$ | interaction parameter |
| $Nu = 2rh/k$ | Nusselt number |
| $P\acute{e} = c_p \rho 2rU/k$ | Péclet number |
| $Pr = \rho\nu c_p/k$ | Prandtl number |
| $Re = Ud/\nu$ | Reynolds number |
| $Rm = \mu\sigma Ud$ | magnetic Reynolds number |

## LIST OF FIGURES

# I. INTRODUCTION

The results of experiments on the aligned-fields magnetohydrodynamic (MHD) flow of mercury past a semi-infinite body are presented in this paper. The experiments were performed in the GALCIT mercury tow tank facility which is described briefly in the following (Sec. 2.1), and more fully in reference 1. Although aligned-fields MHD flow past bodies has been the subject of considerable theoretical work, the solutions which have been found correspond to cases which cannot be realized in the laboratory. This can be seen by comparing the conditions assumed in the various theories with those appropriate to laboratory flows, as has been done by Yonas (Ref. 2). In general, the results of such a comparison show that theoretical studies of MHD flow over bodies treat the fluid as either highly viscous or highly conducting, whereas the liquid metals in which the experiments must be performed are fluids of relatively small kinematic viscosity and electrical conductivity.

The equations of motion for the limits appropriate to the experimental flow are simple in appearance, but the analytic solution of them remains a difficult non-linear problem. The dimensionless equations governing the steady laminar flow of a viscous, incompressible, conducting fluid are (Ref. 3):

$$\nabla \cdot \underline{q} = 0 \qquad (1.1a)$$

$$(\underline{q} \cdot \nabla)\underline{q} = - \nabla p + N(\underline{j} \times B) + \frac{1}{Re} \nabla^2 \underline{q} \qquad (1.1b)$$

$$(\underline{q} \cdot \nabla)\underline{B} - (\underline{B} \cdot \nabla)\underline{q} = \frac{1}{Rm} \nabla^2 \underline{B} \qquad (1.1c)$$

where:*

$$\underline{x} = \frac{\underline{x}^*}{d}, \quad \underline{q} = \frac{\underline{q}^*}{U}, \quad \underline{B} = \frac{\underline{B}^*}{B_o}, \quad \underline{j} = \frac{\underline{j}^*}{\sigma U B_o}, \quad p = \frac{p^* - p_1}{\rho U^2},$$

and starred quantities represent dimensional quantities. The non-dimensional parameters which appear in the equations are:

$Re$ = Reynolds number = $\frac{Ud}{\nu} \sim$ [inertia force/viscous force]

$N$ = interaction parameter = $\frac{\sigma B_o^2}{\rho U} \sim$ [magnetic force/inertia force]

$Rm$ = magnetic Reynolds number = $\mu\sigma Ud \sim$ $\left[\text{body speed/ magnetic diffusion speed}\right]^2$

From these, two other commonly used parameters can be defined:

$M$ = Hartman number = $(NRe)^{\frac{1}{2}} = B_o d (\frac{\sigma}{\rho\nu})^{\frac{1}{2}} \sim$ $\left[\text{magnetic force/ viscous force}\right]^{\frac{1}{2}}$

$\alpha$ = Alfvén number $(\frac{N}{Rm})^{\frac{1}{2}} = \frac{B_o}{U(\rho\mu)^{\frac{1}{2}}} \sim$ [Alfvén speed/body speed]

In the experiments described here, and in other experiments to which reference will later be made, laboratory conditions

---

* The symbols used in this paper are defined in the List of Symbols on p. v.

correspond to:

$$10^3 < \mathrm{Re} < 10^5 \ , \quad 0 \leq N < 10^2, \quad \mathrm{Rm} \begin{cases} << 1 \text{ in Hg} \\ \leq 0(1) \text{ in Na} \end{cases}$$

Therefore, in terms of these parameters, the experimental limits are $\mathrm{Rm} \leq 0(1)$, $\mathrm{Re} >> 1$, and $N << \mathrm{Re}$, whereas the theoretical limits referred to above correspond to $\mathrm{Rm} >> 1$ and $N >> \mathrm{Re}$, $(M >> \mathrm{Re})$.

Two assumptions can be made which simplify the equations governing the experimental flow. The first, that the flow is inviscid, follows from the fact that $\mathrm{Re} >> 1$, and the drag measurements of Suzuki (Ref. 4), which indicate that the flow over this Rankine body under these conditions is laminar and unseparated. The second, that $\underline{B}^* = - B_o \underline{i}$, follows from $\mathrm{Rm} << 1$, using Ampere's law, $\nabla \times \underline{B} = \mathrm{Rm}\ \underline{j}$, and Ohm's law, $\underline{j} = \underline{q} \times \underline{B}$ *, which imply that $\Delta \underline{B} = 0(\mathrm{Rm})$ when $\underline{B}$, $\underline{q} = 0(1)$ **. The induced magnetic fields can, therefore, be neglected, uncoupling the momentum and induction equations and making the current density simply $\underline{j} = - \underline{q} \times \underline{i} = v \underline{i}_\theta$. The equations of motion, in cylindrical coordinates (see Fig. 1), become:

---

* $E = 0$ in axisymmetric flows.

** Although, as stated, this approximation would seem to be reasonable only for mercury flows, it should apply to flows in sodium as well (where $\mathrm{Rm} \leq 0(1)$, because Childress (Ref. 5) has shown that, for $N >> 1$, $\Delta \underline{B} = 0(\mathrm{Rm}/N)$.

$$\frac{\partial u}{\partial x} + \frac{\partial v}{\partial r} + \frac{v}{r} = 0 \qquad (1.2a)$$

$$u \frac{\partial u}{\partial x} + v \frac{\partial u}{\partial r} = - \frac{\partial p}{\partial x} \qquad (1.2b)$$

$$u \frac{\partial v}{\partial x} + v \frac{\partial v}{\partial r} = - \frac{\partial p}{\partial r} - Nv \qquad (1.2c)$$

where, for these experiments, $N \geq O(1)$. For $N >> 1$, the inertia terms in the radial momentum equation may be neglected. The radial pressure gradient is then maintained by the magnetic force. As a result of the ring currents $\underline{j} = v\underline{i}_{\theta}$, the magnetic force both opposes the radial flow and is proportional to it,

A model for this flow in which the currents ahead of the body exist in relatively thin layers concentrated about $r = r_{body} = \frac{1}{2}$ was suggested by Childress (Ref. 6). Yonas (Ref. 2) and Suzuki (Ref. 4) scale the variables in these equations (for $N >> 1$) to show that in such layers, for $p, u = O(1)$ and $O(1) \leq x \leq O(N)$, the equations can be satisfied for $\tilde{r} = r - \frac{1}{2} = O(\sqrt{x/N})$* and $v = j = O(1/\sqrt{Nx})$. These layers would, therefore, extend upstream from the body, growing like $\sqrt{N}$, separating stagnated flow ahead of the body from the freestream flow outside the layers, and merging at $x = O(N)$. Such layer solutions, when found,

---

* Defined in this way, $\tilde{r}$ is a radial coordinate for thin current layers which are centered about $r = \frac{1}{2}$.

would then have to be matched to solutions in adjacent flow regions, including an intermediate upstream region joining the layers at $x = O(N)$ and the flow at upstream infinity. No such solutions have been found, however, since the same non-linear equations (with $\frac{\partial \tilde{p}}{\partial \tilde{r}} = -\tilde{v}$ in scaled variables) apply in the various regions. This current layer model is mentioned here because it makes qualitative predictions about the flow which can be tested by experiments. In Part IV, this model and the Bernoulli law derived by Tamada (Ref. 7) for these flows will be referred to in discussing the results of the experiments.

In 1960, when the GALCIT mercury tow tank facility was constructed, there were no known experimental investigations of these flows. Several experiments have since been performed. Maxworthy (Ref. 8) has measured the drag of freely-falling spheres in liquid sodium, and, more recently (Ref. 9), the pressure distribution around a sphere in a liquid sodium tunnel. Yonas (Ref. 2) has measured the drag of spheres and of a flat disk in the same liquid sodium tunnel. In the GALCIT facility, Ahlstrom (Ref. 10) has measured the magnetic field perturbations produced ahead of a semi-infinite Rankine body, and Suzuki (Ref. 4) has measured the drag on a semi-infinite Rankine body. The results of the above experiments which apply to the flow conditions of the measurements presented in this paper will be discussed in later sections.

Previous experimental investigations of aligned-fields MHD flow past bodies have not provided direct measurements of the actual fluid motions in such flows. The experiments described here were undertaken to provide a description of the fluid motions by means of velocity measurements. These were made using electrically insulated hot-film sensors in the flow ahead of a semi-infinite Rankine body.

# II. DESCRIPTION OF EXPERIMENTS

## 2.1 The Mercury Tow Tank

These experiments were performed in the GALCIT mercury tow tank facility, which is basically a mercury-filled, cylindrical stainless steel tank surrounded by a water-cooled copper solenoid capable of producing steady, axial magnetic fields of up to 12 kilogauss in strength. The tank is mounted with its axis vertical and is 55" long and 5.5" in internal diameter (see Fig. 2). The magnetic fields were calibrated using a Hall-effect probe and found to be uniform axially to 5% and uniform radially to 2% in the middle 25" of the solenoid.

Models are driven through the mercury along the axis of the tank on the end of a 1" outer diameter stainless steel shaft which passes through graphitar bearings at the tank bottom. A system of cables with a magnetic clutch and brake connect the lower end of this drive shaft to a variable speed transmission and an electric motor. The shaft accelerates to a constant velocity within 2" to 3" and can be driven at speeds of up to 3m/sec. The total length of travel was usually from 29" to 36". The drive shaft velocity is measured by a velocity servo which is simply a rotating potentiometer geared to the cable drive so as to produce a voltage output which, when electronically differentiated, is directly proportional to shaft velocity.

A detailed description of this facility may be found in reference 1.

## 2.2 The Hot-Film Sensor

The practical problems of velocity measurement in mercury are extremely difficult. To be successful a sensor must be electrically insulated, able to withstand prolonged exposure to a mercury environment, reasonably rugged, and capable of giving satisfactory response to velocity changes in a low Prandtl number fluid. Preliminary work done with enamel and epoxy-coated wires similar to those used by Sajben (Ref. 11), sensors of thermistor material of the kind used by Lumley (Ref. 12), and quartz-coated, hot-film sensors*, led to selection of the latter as having the most promise. At the time, hot-film sensors had apparently not been used for measurements in liquid metals, although Malcolm (Ref. 13) has recently reported their successful application to the measurement of turbulence intensities in mercury.

The hot-film sensor is shown in figure 3. A platinum film of approximately $10^3$ Å thickness is deposited onto a .002" diameter quartz cylinder and insulated with a sputtered quartz coating approximately $1.6 \times 10^4$ Å thick. The cylinder has an overall length of .080", and a sensitive length of .040". The length-to-diameter ratio is therefore

---

* Manufactured by Thermo-Systems, Inc., Minneapolis, Minnesota.

20 to 1. It is supported by epoxy-coated needles which are mounted on the end of a .125" diameter stainless steel shaft. The opposite end of the shaft has an O-ring seal and gold-plated electrical contact pins so that the probe may be attached to various holders with a mercury-tight fit. The temperature coefficient of resistance of each sensor was found experimentally, a typical value being $.00256^{\circ}C^{-1}$.

The sensor was operated in the constant-temperature mode. Sensors of this type have inferior accuracy and frequency response when operated at constant-current due to the large thermal inertia of the boundary layer and the inactive coating and substrate.

## 2.3 Experimental Procedure

The model used for these experiments was a lucite Rankine halfbody mounted on the end of the tow tank drive shaft to simulate a semi-infinite body. This body shape, which is defined by a source in a uniform stream, was chosen because the magnetic field induced by it had been measured previously by Ahlstrom (Ref. 10), and the drag force on it had been measured previously by Suzuki (Ref. 4). Their choice of the Rankine halfbody was motivated primarily by the simple analytical form of its potential flow.

Velocity along the flow centerline ahead of the body was measured by mounting the hot-film sensor in two ways. Measurements were made with the sensor at the lower end of a .180" diameter stainless steel probe, which was suspended above the free surface of the mercury at the top of the tow tank (see Fig. 4a). The holder to which the upper half of the probe's 24" length was attached, allowed the probe to be moved vertically or horizontally for positioning of the sensor in the mercury, and held it firmly in place when positioned. The range of horizontal sensor movement was limited to $r \leq 1.25"$. When mounted in this way, the sensor measured the flow velocity induced by the approaching model, at a fixed point in the laboratory reference frame.

Measurements were also made with the sensor at the end of another .180" diameter stainless steel probe which was attached to the end of the tow tank drive shaft (see Fig. 4b). In this arrangement the electrical connections were made by means of a cable brought up through the hollow drive shaft. A Rankine body headform was then fitted to the end of the sting so that, again, the sting and model formed a semi-infinite body, this time with the sensor and probe mounted on the body. The distance between the sensor and body stagnation point was adjusted by means of cylindrical sections of various lengths which were put between the end of the drive shaft and the model headform. In this way velocity measurements were made with the sensor at a fixed position ahead of the body during the entire course of a run.

The sensor was operated at constant temperature using a Thermo-Systems Model 1000 A anemometer. The anemometer signal was fed through a voltage-to-frequency converter to a digital counter so that fluctuations as small as one part in ten-thousand could be monitored. During the course of a run, the outputs from the anemometer and the drive shaft velocity servo were displayed simultaneously on a dual-beam oscilloscope and their traces recorded photographically.

The actual operating procedure used during the course of the experiments was determined primarily by the unique difficulties encountered when hot-films of this kind are used in liquid mercury. It is impossible to keep a free surface of mercury perfectly clean, and when a sensor is passed through such a surface the quartz insulation, which is not wetted by the mercury, picks up a coating of impurities. The hot-film is then effectively surrounded by both a layer of quartz and another layer of unknown composition. As long as this impurity coating remains unchanged, its effect on the performance of the sensor is not bothersome. This is the case during the course of a given immersion, except that even at zero velocity and constant temperature the anemometer signal may exhibit a slow drift. The possible occurrence of this kind of drift, which Sajben (Ref. 11) attributes to the presence of minute amounts of impurities within the mercury, was one reason the anemometer signal was accurately monitored at all times.

More important is the fact that the properties of the impurity coating may change significantly each time the sensor is passed through the mercury surface. As a result, a sensor operated under otherwise identical conditions during different immersions, may perform as though the sensor-to-fluid temperature difference, or overheat, had been altered. Although this effect of the impurity coating can be eliminated by calibrating in terms of the difference between heat transfer at any velocity and that at some reference velocity (zero velocity was used, see Sec. 2.4), such a calibration will be in error unless both measurements used to calculate the difference are made under conditions for which only the velocity has changed. In particular, quantities such as the properties of the sensor impurity coating and the fluid temperature, as well as the various directly-controllable quantities involved, must be identical (see Sec. 3.2 and the Appendix). To insure that this was the case, the mercury temperature and the anemometer signal for zero velocity were measured before and after every run. In addition, a vacuum skimmer was used to clean the mercury surface before removing or inserting the sensor, and the number of times the sensor was passed through the surface was kept at a minimum. Finally, whenever possible, the sensor was recalibrated after each new immersion.

### 2.3.1 Sensor Mounted on Tow Tank

The only important difference between calibration runs and data runs was the presence of the magnetic field during the latter. When measurements were made with the sensor mounted at the top of the tank, the sensor was calibrated using the rising displacement flow produced in the mercury by the drive shaft as it entered from below. The velocity profile of this flow was measured and found to be quite flat at the level of the sensor (see Fig. 5). The velocity of the displacement flow was calculated using the measured drive shaft velocity and the cross-sectional areas of the tank and the drive shaft. In this way the sensor was calibrated over a velocity range of from 0.3 cm/sec to 4cm/sec. When data runs were made with the sensor mounted in this way and positioned within one body radius of the tow tank centerline, the drive shaft stops were set so that the stagnation point of the Rankine body was 0.5" from the sensor at the end of each run. For this reason, measurements of the potential flow of the Rankine body at zero magnetic field were of little value, for while they reproduced the known velocity profile to within 0.5" of the stagnation point, more than 85% of the overall velocity change in the potential flow velocity field occurs in the final 0.5". At low speeds it was possible to allow the shaft to run directly into these solid stops, but at higher speeds a flip-stop was required to allow the shaft to decelerate before impacting the solid stops. When used, the flip-stop was located 2" ahead of the solid stops so that useful data were obtained only to within 2.5" of the model. During runs for which the sensor was positioned more than one body radius off the tank centerline, the body was allowed to travel past the sensor. The distance between the model and the sensor was measured when the sensor was first mounted in the tank. It was known thereafter by means of a calibrated scale along which the lower end of the drive shaft traveled. Readings on this scale provided the initial conditions from which the relative positions of the model and sensor during a run were calculated (see Sec.2.4).

When the magnetic field was turned on, the temperature of the entire system rose due to the heat generated in the solenoid. This temperature change was monitored using thermocouples at various locations in the solenoid cooling system, and the sensor itself in the mercury. It was found that waiting periods of well over an hour were required to assure that the temperature of the system had completely stabilized. After taking data over the full range of drive-shaft velocities, the magnetic field was turned off and the system was allowed to return to room temperature. The sensor was then re-calibrated before it was removed from the mercury. This procedure was followed for each value of the magnetic field.

When measurements were made with the single sensor offset radially from the flow centerline, runs were made with it oriented both parallel and perpendicular to the tank radius as a check on the possible effects of whatever small radial velocity was present.

Typical oscilloscope traces for measurements made in this way are shown in figure 6.

### 2.3.2 Sensor Mounted on Drive Shaft

When the sensor was mounted on the drive shaft, it was positioned from 4" to 10" ahead of the body for all calibration runs. The velocity at the sensor was assumed to be that of the drive shaft minus that of the displacement flow. This assumption is supported by zero field measurements which show no change in displacement flow velocity as the model approached to within 4" of the tank-mounted sensor and by the fact that the potential flow disturbance is less than 0.4% of the body speed at a distance of 4". The calibration velocity range was from 2.5 cm/sec to more than 20 cm/sec.

Data were taken at a fixed value of the magnetic field for the full range of velocities at each of 5 sensor positions: 4", 3", 2", 1" and 0.5" ahead of the body stagnation point. This involved removing the sensor each time its position was changed. Data were also taken with the sensor at one fixed position ahead of the body for a range of velocities at each of several values of the magnetic field. This produced measurements at one position over the full range of flow conditions without passing the sensor through the mercury surface, but was extremely inefficient due to the number of time-consuming magnetic field changes required. Only enough runs were made using this latter procedure to confirm that the difference between the data from the two procedures was not greater than the uncertainty in the calibration itself. This indicates that the frequent immersions did not tend to produce a more unstable impurity layer which could change significantly during the course of a run.

Typical oscilloscope traces for measurements made with the sensor mounted on the drive shaft are shown in figure 7.

For these experiments the range of body velocities was from about 2 cm/sec to over 20 cm/sec. The magnetic fields used were 4,500, 6,800, 9,000 and 11,300 gauss. The ranges of the basic dimensionless parameters were therefore as follows:

$5 \times 10^3 \leq Re \leq 9 \times 10^4$ , $7 \times 10^{-4} \leq Rm \leq 1 \times 10^{-2}$ ,

$4 \leq N \leq 84$, and for all runs $\alpha > 1$.

## 2.4 Heat Transfer Relations and Data Reduction

For the case of a very long, uniformly-heated cylinder in a steady, uniform flow perpendicular to its axis, the equation for the rate of heat transfer can be written:

$$q = h\,A\,(T_{surface} - T_{fluid}) \qquad (2.1)$$

where h is the heat transfer coefficient, a function of the composition of the fluid and the nature of the flow, and A is the surface area. $T_{surface}$ is considered constant and is greater than $T_{fluid}$. In terms of Nusselt number, defined as $Nu = \frac{2rh}{k_f}$, the non-dimensional heat transfer coefficient for a cylinder in forced convection, this becomes:

$$\frac{q}{L} = \pi k_f Nu \ (T_{surface} - T_{fluid}) \tag{2.2}$$

where L is the cylinder length and $k_f$ is the thermal conductivity of the fluid. For low Pr flows in which the effects of free convection and viscous dissipation can be neglected, Nu is a function of the Péclet number Pé = Pr Re $= \frac{c_p \rho 2rU}{k}$, the ratio of the flow speed and the thermal diffusion speed. Equation (2.2) is also valid for a heated cylinder which is surrounded by one or more layers of insulation, as long as $T_{surface}$ is the temperature of the outer surface of such a composite cylinder. For the sensor used in these experiments, $T_{surface}$ is unknown and depends upon the physical properties of the impurity coating, which may vary. It is $T_{film}$, the temperature of the platinum film at $r = r_{film}$, which is known and held constant. Solving the heat conduction equation in cylindrical coordinates for steady state heat transfer with surfaces maintained at steady temperatures, and using Fourier's law, one obtains

$$\frac{q}{L} = \frac{2\pi k (T_{inner} - T_{outer})}{\ell n (r_{outer}/r_{inner})} \tag{2.3}$$

for the rate of heat transfer across surfaces within

$r_{inner} \leq r \leq r_{outer}$ with $T_{inner} > T_{outer}$. Writing this for surfaces within the quartz coating and within the impurity layer, and equating with equation (2.2), since the heat transfer through all such surfaces must be equal, one obtains after re-arranging terms (see Chapman, Ref. 14),

$$\frac{\pi k_f L(T_{film} - T_{fluid})}{q} = \frac{1}{Nu} + \frac{1}{2}\frac{k_f}{k_c}\ell n(r_c/r_{film}) + \frac{1}{2}\frac{k_f}{k_i}\ell n(r_i/r_c) \qquad (2.4)$$

The subscripts c and f refer to the quartz coating and the fluid, respectively. From this equation it can be seen that even for a fixed film-to-fluid temperature difference and constant fluid properties, changes in the measured quantities on the left-hand side correspond to changes in the velocity dependent term, $1/Nu(P\acute{e})$, only if the two right-hand terms, which depend on the properties of the insulating layers, are constant. Sajben (Ref. 11) has shown that these velocity independent terms can be eliminated by defining:

$$X(P\acute{e}) = \left[\pi k_f L(T_{film} - T_{fluid})\right]\left[\frac{1}{q(0)} - \frac{1}{q(P\acute{e})}\right] = \frac{1}{Nu(0)} - \frac{1}{Nu(P\acute{e})} \qquad (2.5)$$

A calibration in terms of $X(P\acute{e})$ vs. $P\acute{e}$ does not depend on the properties of the insulating layers as long as each $X(P\acute{e})$ value is calculated using a pair of measurements at

Pė = 0 and Pė ≠ 0 for which the properties of the layers are identical. In addition, each pair of measurements must be made at the same film-to-fluid temperature difference and at the same fluid temperature.

The calculations of X(Pė) from the data obtained in each run was straightforward. The voltage across the sensor was found using the measured anemometer output voltage and the known resistances of the circuit, probe, and leads with which the sensor was in series. X(Pė) was then obtained using the ohmic dissipation calculated from the sensor voltage and resistance. Because a computer was used to calculate X(Pė), Pė, and all other flow parameters, it was possible to evaluate them using the values of the fluid properties which corresponded to the measured temperature of each run. Calibration curves were used to find Pė using the values of X(Pė) determined from the quantities measured during the data runs. X(Pė) vs. Pė calibrations for two velocity ranges are shown in figures 8 and 9.

The drive shaft velocity was known from the output of the velocity servo. For calibration runs this was a measure of the flow velocity past the sensor. For all runs it was a measure of the freestream flow of mercury past the model. In each case it was necessary to correct the drive shaft velocity to account for the dispacement flow in tank (see Sec. 2.3 and the Appendix).

The velocity measured by the sensor, the velocity of the displacement flow, and the velocity of the drive shaft were used to calculate a normalized velocity, u, such that u = 0 in the undisturbed displacement flow and u = 1 at the body stagnation point. In a tow tank without a displacement flow, u would be the ratio of flow velocity to body velocity measured by an observer fixed in the laboratory coordinate system. It is the normalized form of the velocity perturbation produced by the moving body. For measurements made with the sensor mounted at the top of the tow tank,

$$u = \frac{P\acute{e}_{\text{measured}} - P\acute{e}_{\text{displ. flow}}}{P\acute{e}_{\text{drive shaft}} - P\acute{e}_{\text{displ. flow}}} \tag{2.6}$$

For measurements made with the sensor mounted on the drive shaft,

$$u = \frac{P\acute{e}_{\text{drive shaft}} - P\acute{e}_{\text{measured}} - P\acute{e}_{\text{displ. flow}}}{P\acute{e}_{\text{drive shaft}} - P\acute{e}_{\text{displ. flow}}} \tag{2.7}$$

When runs were made with the sensor mounted at the top of the tow tank, the relative position of the sensor and the body was determined by using the drive shaft velocity and the time scale of the oscilloscope trace to calculate distance from the known starting conditions. Each of these runs produced data from which a full profile of flow velocity versus axial distance could be obtained. When the sensor was mounted on the drive shaft the distance between it and the body was fixed and measured directly. Each run made in this way supplied data leading to only one point in such a profile.

# III. RESULTS OF EXPERIMENTS

## 3.1 Actual Results

Results of typical measurements of axial velocity on the flow centerline ahead of the Rankine body which were made with the sensor mounted at the top of the tow tank, are shown in figure 10. The normalized velocity, u, (Sec. 2.4) is plotted as a function of distance in body diameters from the body stagnation point for various values of the interaction parameter. The zero magnetic field Rankine body axial velocity profile is included for comparison. The measurements made with the sensor mounted on the drive shaft did not provide complete profiles of this kind because each run produced a data point at a slightly different value of the interaction parameter, and the range of distances from the body was not as great.

The axial length of the upstream influence of the body for each value of the interaction parameter was characterized by the arbitrarily chosen distance between the point in the velocity profile at which u = .05 and the body stagnation point. Figure 11 shows this length plotted as a function of the interaction parameter. The correlation with N alone was not unexpected, for it is indicated by the equations of Part I and was found in the drag measurements of both Suzuki (Ref. 4) and Yonas (Ref. 2). Lines of slope N and $N^{\frac{1}{2}}$ are plotted in figure 11, from which it can be seen that the disturbance length defined in this way is directly proportional to $N^{\frac{1}{2}}$.

The dependence of this length on $N^{\frac{1}{2}}$ suggests the use of $x_b/N^{\frac{1}{2}}$ as a new length scale. In figure 12, the results of velocity measurements made with the sensor mounted at the top of the tow tank and on the drive shaft are shown as functions of $x_b/N^{\frac{1}{2}}$. Although the data in the figure were obtained over ranges of more than an order of magnitude in both N and Re, they form a single u vs. $x_b/N^{\frac{1}{2}}$ profile. The solid symbols represent the results of measurements made with the sensor mounted on the drive shaft, and lie within $0 < x_b/N^{\frac{1}{2}} < 1.5$, which corresponds to more than 85% of the velocity change from 1 to 0. All other symbols represent the results of measurements made with the sensor mounted on the tow tank. They lie in the range $0.5 < x_b/N^{\frac{1}{2}} < 4.0$, which corresponds to 50% of the velocity change from 0 to 1, so that a portion of the profile corresponding to approximately 35% of the total change in velocity is produced by the overlap of the two kinds of data.

In figure 13, the full profile is shown in a semi-logarithmic plot. Except for small $x_b/N^{\frac{1}{2}}$, the data describe a straight line, which on such a plot indicates exponential behavior. Away from the body, the axial velocity perturbations produced by it become exponentially small.

The results of the measurements made with the sensor tank-mounted at radial positions other than $r = 0$, were first prepared in a form similar to that of figure 10. For each value of N, a series of curves representing u vs. $x_b$ at each radial station was prepared. An example of such a plot is shown in figure 14. The interpretation of the measured quantity as the axial flow velocity is discussed in section 3.2. A great deal of data of this kind were obtained over the full range of experimental conditions, and a series of plots such as that in figure 14 was obtained. By cross-plotting these data it was possible to produce profiles of the axial velocity at various distances ahead of the Rankine body as shown in figure 15. Sets of profiles were obtained for values of N ranging from 11 to 47. These are shown in figure 16. The bars on the curves in figure 16 indicate the scatter in the data used to define the curves.

The regions of the flow field in which velocities have been measured are: from $x_b >> 1$ (far upstream) to within $x_b = 0.5$ on $r - 0$; from $x_b >> 1$ to within $x_b = 3$ for $0 < r \leq 0.5$; and from $x_b >> 1$ to $x_b < -2$ for $0.5 < r < 1.25$.

## 3.2 Discussion of Uncertainties

This section presents a review of the estimates arrived at in the Appendix. There, the uncertainties associated with the directly-measured quantities are used to provide estimates of the uncertainties in the final results of the experiments.

Each value of the calibration parameter X(Pé) $\propto\left(\frac{\Delta T}{q(0)} - \frac{\Delta T}{q(\text{Pé})}\right)$, was calculated using a pair of measurements made at different flow velocities, under the assumption that all other conditions were constant. The uncertainty in X(Pé), therefore, depends not only upon the accuracy of the individual measurements, but also upon the amount by which the presumably constant conditions could have differed for a given pair of measurements. By considering the extent to which these conditions* could have changed, and the effects of such changes on X(Pé), the average uncertainty in X(Pé) is estimated to be ± 6%. The scatter in the calibration curves, which is a measure of this same quantity, is of order ± 5%.

Over most of the velocity range, when X(Pé) is used with the calibration curves to determine Pë, the resulting average uncertainty in the latter is ± 7%. At the highest velocities, where X(Pé) becomes an increasingly weak function of Pé, this increases to the order of ± 15% to ± 20%.

The uncertainty in the normalized velocity, u, depends almost entirely on that associated with the Pé determined from the calibration curves. It varies according to the relative magnitudes of u and Pé, and the way in which u is calculated. Most of the data were obtained using the sensor mounted on the tow tank. These estimates indicate

---

* The important conditions are the mercury temperature and the sensor coating conditions.

that the values of u calculated from such data are accurate to within ± 8%, except for the smallest values ($u \leq 0(10^{-2})$), which are known only to within ± 10% to ± 40%, depending on their magnitude. The estimated uncertainty of the normalized velocities calculated from the shaft-mounted sensor data varies from less than ± 7% to ± 15%, except for a few values which are marked with error flags in the figures and are discussed in the Appendix.

The sensor-to-body distances, for the data taken with the sensor mounted on the tow tank, could be calculated to within ± 4% for any given drive shaft speed. The relative position of the origin for different drive shaft speeds, however, could only be determined to within ± 0.2 body diameters. The effect of this is to increase the possibility of scatter in data obtained at equal values of N using different drive shaft speeds.

When the sensor was used at radial positions other than that of the flow centerline, the signal was assumed to be related to only the axial component of velocity. As discussed in the Appendix, this assumption was based on the fact that these sensors are insensitive to flow yaw angle in low Re mercury flows, and that in the experimental flow $v \ll u$. The assumption appears justified in view of the experimental results. They show that the data were not dependent on whether the sensor was perpendicular or parallel to the radial velocity, that the measured flow could satisfy the continuity equation, and that v, as inferred from the axial velocity data, satifies $v << u$.

Finally, it should be mentioned here that during the course of the experiments, operating procedures such as the sequence of sensor positions and controllable flow conditions were varied so as to assure against the possibility of systematic errors in the results. It addition, it should also be noted that the profile defined by the data in figure 12 (u vs. $x_b/N^{\frac{1}{2}}$), is produced by the overlapping of results which were obtained for widely different experimental conditions, and therefore depend in different ways upon the uncertainties in any one measurement. The fact that the agreement between them is quite good indicates that systematic errors are not present.

### 3.3 Flow Conditions in the Tow Tank

The degree to which the experimental flow can be considered a steady one will be considered first. In one sense the flow in the tow tank was never steady because the model was always approaching the free surface at the top of the tank. On the other hand, the results of several measurements lead to the conclusion that when the experimental flow was studied, it was in a steady state in the sense that it had become fully developed after its initiation.The results of the runs made with the sensor mounted on the drive shaft are one indication that this was true. They show that the velocity ahead of the body reached a constant value which was maintained throughout most of each run (see Fig. 7). In addition, experiments were performed, using a tank-mounted sensor, in which the starting distance (i.e., the distance between the model stagnation point and the sensor at the start of a run), was varied from 11 to 29 body diameters. The results of these experiments are shown in figure 17. For initial positions greater than 17, the data do not depend on starting position, whereas the starting position for all of the regular experiments was 29 body diameters. The measurements of magnetic field perturbations by Ahlstrom (Ref. 10) for $0.6 < N < 4$, and the measurements of drag by Suzuki (Ref. 4) for $0 < N < 20$, made in the same facility, tend to confirm the conclusion that the experimental flow was fully established. Ahlstrom found that his results were independent of starting position for initial distances greater than 15, and Suzuki found that the drag force was constant during most of each run.

The constraint imposed by the wall boundary conditions cannot have had a significant effect on the velocity field in the tow tank. Potential flow past a Rankine body in an unbounded fluid corresponds to a maximum radial velocity at $r = r_{wall}$ (= 2.75 body dia.) of only .008. The introduction of the magnetic force, which acts to suppress radial velocities, should reduce this further so that to a very good approximation at the values of N used here, an unbounded flow would satisfy these experimental boundary conditions.

The other velocity boundary condition which must be considered is that imposed by the free surface at the top of the tow tank. Its influence must increase with increased N, since the length of the disturbance in front of the body increases with N. During all of the normal experiments which used a tank-mounted sensor, the sensor was located 7½ body diameters beneath the mercury surface. Additional experiments were performed in which all conditions were duplicated, including the position of the sensor with respect to the tow tank, except that the distance between the sensor and the mercury surface was varied by changing the mercury level in the tow tank. The results of these measurements are shown in figure 18 for distances of 2, 4½, 7½ and $8\frac{1}{8}$ body diameters. For this range of surface positions the results are independent of surface position for the whole range of N.

The length of the upstream disturbance (as defined in Sec. 3.1), varies from about 5 body diameters at $N \sim 4.5$ to 15 body diameters at $N \sim 45$, increasing as $N^{\frac{1}{2}}$. The data taken in the normal way (with the surface 7½ body diameters above the sensor), produced velocity profiles which extend to within 4 to 5 body diameters of the stagnation point, so that all such data were obtained while the body was approximately 12 diameters or more away from the mercury surface. Only for values of N greater than about 25 was the disturbance length greater than 12 diameters. Therefore, most of the "normal" data were obtained while the body was at a distance from the surface greater than this disturbance length. On the other hand, nearly all of the data produced at the lowest surface levels were obtained while the upstream disturbance, so defined, was near enough to be interacting with the free surface. The results were the same for all these cases. If the flow ahead of the body had been significantly altered due to its interaction with the mercury surface, the effects should have become apparent when the normal results for the full range of N were plotted together in the form u vs. $x_b/N^{\frac{1}{2}}$, as well as when the data for different surface levels were plotted in figure 18. In view of the actual results of these measurements, it must be concluded that during the experiments the body did not come near enough to the free surface for the latter to seriously affect the velocity field at the sensor position.

Finally, it should be pointed out that due to the fluid displaced by the drive shaft, the flow in the tow tank is not strictly equivalent to freestream flow past a stationary body. As a result, the normalized velocity, u, referred to the displacement flow ahead of the body (u = 0), becomes negative downstream of the body (u = - .03), where the velocity relative to the tow tank is zero.

## IV. DISCUSSION OF RESULTS

In this Part, the experimental results are used to provide a reasonably complete description of this MHD flow. In so doing, the approximations and equations of motion presented in Part I are assumed to apply. The measurements, the implications which can be drawn from them, and some results available from previous investigations of such flows, are discussed in the process. The flow model presented is rather qualitative and is based on physical arguments more than mathematical analysis. As mentioned in Part I, there are no theoretical solutions which apply in the limits appropriate to the experimental flow.

The experiments show that, compared to the zero field potential flow, the MHD flow for $N \geq 0(1)$ has a large upstream disturbance extending far ahead of the body. The length of the disturbance, which grows as $N^{\frac{1}{2}}$, is 10 to 20 body diameters for the highest values of N used here.* On the other hand, the centerline velocity profiles show that only very much nearer the body is the fluid motion relative to the body actually reduced to the extent that it can be considered stagnated. Such flow did exist, however, just ahead of the body, as was dramatically demonstrated by the shaft-mounted sensor measurements. Although the sensor was sensitive to velocities as small as a few per cent of the

---

* The corresponding length for flow at $N = 0$ is 0.85 body diameters.

drive shaft velocity, it produced a steady, zero-velocity signal when mounted 0.5" ahead of the body at $N \geqslant 17$, and when mounted 1" ahead of the body at $N \geqslant 35$. The measurements do not provide sufficient data to describe the dependence of the length and shape of this stagnated portion of the flow on N. However, they do show that the flow ahead of the body consists of a relatively short region of stagnant fluid preceded by a much longer region in which the fluid velocity rapidly approaches that of the freestream flow. Only if the former grows as $N^{\frac{1}{2}}$, will the correlation of u and $x_b/N^{\frac{1}{2}}$ in figure 12 remain valid for all N. The stagnated region, however, could be increasing in length at a faster rate, such as directly with N. In such a case, for increased N, the transition from zero to freestream velocity would have to take place within a region no longer similar to the one measured here, or within one in which the distance, $x_b$, is referred to the front of the stagnant region and not to the body. Such departures of the flow pattern from that measured in these experiments, could only occur for values of N much greater than those obtained here. They would imply that the limiting flow for $N \to \infty$ is approached only very slowly - even as N is increased by orders of magnitude.

The full axial velocity results show that, with increased N, the magnitude of the velocity defect at a fixed point ahead of the body increases on and near the flow centerline. It increases more slowly, or may even decrease, at larger radial positions. In other words, at the same time that the total velocity defect increases, it also becomes more concentrated about the axis of symmetry. If the radial position at which the defect is one-half its maximum is used as a measure of the width of each velocity defect profile, the width of the disturbance slowly decreases at a fixed axial position as N is increased. For a fixed N, it grows very slowly with increased distance from the body.

An indication of the current distribution can be obtained using the fact that the current density at a point in the flow is just proportional to the radial velocity at that point (see Part I). The average radial velocity between $x_b$ and $x_b + 1$ at r was calculated by graphically integrating the continuity equation $v = -\frac{1}{r}\int_0^r \frac{\partial u}{\partial x} r \partial r$, using the profiles of axial velocity to provide $\frac{\partial u}{\partial x}$. The results, shown in figure 19, provide an estimate of the magnitude and distribution of v and j. These quantities increase from zero at $r = 0$ almost linearly with r, reflecting the weak r-dependence of $\frac{\partial u}{\partial x}$ for small r. As $r \to 0(1)$, the current density and radial velocity reach maximums and then decrease with further increases in r. Typical radial velocities in the flow are an order of magnitude smaller than the characteristic velocity defect at the same axial position.

These experimental results provide the magnitude and distribution of u, v, and j in the flow ahead of the body for $N > 10$. The current layer model mentioned in Part I describes these same quantities in the same flow region under the assumption that $N >> 1$. In the model flow, there exist well-defined current layers, centered about $r = \frac{1}{2}$, which maintain the radial pressure gradient necessary to separate the outer freestream flow from a slug of nearly stagnated fluid ahead of the body. The merging of the layers, which terminates the stagnant region, takes place a distance $x = O(N)$ ahead of the body. In the limit $N \to \infty$, for $N/Re \to 0$, the model flow becomes undisturbed freestream flow past an infinitely long slug of fluid bounded by infinitesimally thin current sheets. Therefore, while the measured flow does not preclude the possibility of such a limiting form, it does not fit the current layer model. Instead of well-defined current layers, there are broad regions of maximum current density. The length of the upstream disturbance grows as $N^{\frac{1}{2}}$. The small portion of it which contains stagnated flow grows with N at an undetermined rate, but is definitely not of $O(N)$ in length. Although the entire disturbance becomes more "slug-like" in that it becomes more concentrated about $r = 0$ as N increases, it is not a slug of very slowly moving fluid. The current layer model describes a region containing a slug of stagnant fluid bounded by current layers, but provides no description of the intermediate region which must exist between the slug and the upstream fluid. In the measured flow it is found that the stagnant region, which could not be measured in detail, is short, and that most of the disturbance consists of a region of transition from zero to freestream velocity.

The experimental flow can be described further by referring to the generalized Bernoulli law for inviscid, MHD flows derived by Tamada (Ref. 7),

$$\underline{q} \cdot \nabla H = \underline{q} \cdot \nabla\left[\frac{1}{2}\ (u^2 + v^2) + p\right]$$

$$= N\underline{q} \cdot (\underline{j} \times \underline{B}) = -N\underline{j}^2 \qquad (4.1)$$

The Bernoulli function $H = \frac{1}{2}\ (u^2 + v^2) + p$, is constant along streamlines on which $\underline{j} = 0$, and must decrease along all streamlines on which $\underline{j} \neq 0$. This means that since $v \sim j$, closed streamlines are not possible in steady flow, and also that the maximum pressure in the flow in normal stagnation pressure ($P_o = \frac{1}{2}$ in this notation), at the stagnation point. In both the non-magnetic and MHD flows, the static pressure along $r = 0$ rises from its freestream value (zero) to this stagnation pressure at the body. In both cases the axial pressure gradient is balanced only by the axial fluid deceleration. The difference between the two flows appears in the radial equation of motion. Radial pressure gradients in the ordinary flow can only be supported by the inertia terms, but in the MHD flow for $N \gg 1$ these may be neglected, so that the equation becomes

$\frac{\partial p}{\partial r} \simeq - Nv$. The ability of the radial flow to support a radial pressure gradient is enhanced, while the net radial flux of fluid remains unchanged (for a given freestream velocity), and the maximum possible radial pressure drop from $r = 0$ to $r \gg 1$ is constant. Qualitatively, then, the magnetic force which acts on the fluid when it crosses field lines, tends to decrease the radial flow near the body and increase it away from the body. Thus, it straightens the streamlines and increases the axial distance over which the pressure rises from $p = 0$ upstream to $p \leq \frac{1}{2}$ at the body.

Along the axis of the flow $v = j = 0$, and the Bernoulli function is constant, $H = \frac{1}{2}$, so that the local pressure is directly related to the known axial velocity, $p(x, 0) = \frac{1}{2} - \frac{\tilde{U}^2(x, 0)}{2}$.* Therefore, the pressure change along $r = 0$ occurs over an axial distance proportional to $N^{\frac{1}{2}}$. An example of this pressure profile for $N = 29$ is shown in figure 20, along with the corresponding profile for potential flow.

The pressure difference which exists between $r = 0$ and the flow at large r is maintained by the net magnetic force, $- N \int_0^r v(x, r)\, \partial r$, at x. Lacking an analytical expression for the distribution of radial velocity, the area under the

---

* The results of the experiments are presented in terms of the normalized velocity defect in the freestream flow, so that the velocity referred to above is $\tilde{U} = 1 - u_{defect}$, and is the normalized fluid velocity relative to the body.

velocity profiles of figure 19 can be used to provide an estimate of the magnitude of this force. For example, at N = 29, the values estimated in this way are .36 at $x_b$ = 5, .26 at $x_b$ = 6, and .145 at $x_b$ = 8. The corresponding changes in pressure from figure 20, assuming p = 0 in the outer flow, are approximately .24, .18 and .13.* These admittedly crude estimates are cited only to demonstrate that the radial velocities which correspond to the measured axial velocity profiles are of the correct order, and sufficient, to support the radial pressure gradients which must exist in the flow.

It may be noted here that had the radial velocities been confined to relatively thin layers, their maximum values (which were .017, .012 and .006 at the positions referred to above for N = 29), would have had to have been considerably higher at the same axial positions and same N. And, finally, that if layers of some kind are assumed to exist very near the body where there is a region of stagnated fluid, they must be able to support a radial pressure change of order 0.5. Given an estimate of the thickness of the layers in this region, an approximate mean velocity

---

* These values should be slightly low because in the outer flow $p \to -.03$ downstream of the body due to the blockage effect of the body in the tow tank.

through them would then be known.* However, despite the fact that near the body the distribution of radial velocity must become reasonably concentrated around $r = \frac{1}{2}$, the flow in this region (where the stagnated flow, the curved body face, and the outer flow come together) is certainly too complex to be described in terms of a simple current layer.

The effects of the Joule dissipation on the pressure and velocity in the flow can be considered by referring again to the Bernoulli law (Eq. 4.1). The stagnation pressure, $P_o = p + \left(\frac{u^2 + v^2}{2}\right)$, is decreased on all streamlines which have passed through regions of non-zero current density. The decrease at any point in the flow is equal to the total Joule dissipation which has occurred upstream of the point along the streamline passing through it,

$$\Delta P_o = - N \int j^2 \, ds = - N \int v^2 \, ds \; .$$

Since the stagnation pressure can only decrease, and the amount of Joule dissipation which occurs along different streamlines varies, radial as well as axial stagnation pressure gradients occur in the flow. At axial positions ahead of the body the stagnation pressure falls from $\frac{1}{2}$ on $r = 0$ to lower values at $r > 0$, in the region where stream-

---

* For example, a mean radial velocity of $\sim .09$ would be required for $N = 29$ through layers of thickness $\Delta r \sim 1/N^{\frac{1}{2}}$ $\sim .18$ - the thickness at $x \sim 0(1)$ which results from the order of magnitude arguments used in the current layer model.

lines pass which have undergone dissipation, and then rises again to $\frac{1}{2}$ at large r where there are streamlines on which the radial velocity has been continuously zero. As shown by Tamada (Ref. 7), far downstream of the body, where the flow again becomes uniform in the sense that $v = 0$, there can be no radial static pressure gradient and the axial velocity must be directly related to the stagnation pressure. Due to the loss in stagnation pressure suffered by the flow along streamlines which have experienced Joule dissipation, the axial velocities near the body are lower than those in the flow far from the body. This vortical wake does not diffuse or dissipate in inviscid flow. Looked at in terms of vorticity and the equation for the change in vorticity along a streamline, $\frac{d\omega_\theta}{ds} = - N \frac{\partial v}{\partial x}$, this means that the vorticity in the direction created by the positive $\frac{\partial v}{\partial x}$ in the flow ahead of the body, is greater than the vorticity suppressed near the body where $\frac{\partial v}{\partial x}$ becomes negative. For Re large, but not infinite, this wake will ultimately diffuse to produce uniform flow far downstream.

Because of the stagnation pressure variations in the flow, the velocity measurements cannot be used directly to determine static pressures. This is particularly true over the front of the body near $r = \frac{1}{2}$ where the stagnation pressure must be close to its minimum value. Measurements of static and stagnation pressures over the surface of a sphere in aligned-fields MHD flow, for $1.5 < N < 40$, have been made by Maxworthy (Ref. 9). These show that the stagnation pressure in the flow past the sphere, at the position corresponding to $r = \frac{1}{2}$ on the halfbody used here, is from 40% to 90% less than its freestream value and decreases as $N^{\frac{1}{2}}$. At the same position, static pressures are found to be of $0(1)$ and negative, so that the corresponding velocities must be greater than freestream by as much as 50%. The resultant net pressure force on the front of the sphere rises only to about $C_D = 0.5$ at $N \sim 12$, and then falls toward zero as N is increased further, due to the effect of the increasingly large contribution of the negative pressure. In addition, large negative pressures near the body can only exist if maintained by a magnetic force, so that the flow past the body must contain negative radial velocities. These results are cited to demonstrate the possible effects of the stagnation pressure losses due to Joule dissipation in such flows, and to introduce a discussion of whether such an effect could occur in the flow under consideration here.

Suzuki (Ref. 4) has measured the drag of a Rankine halfbody in these flows. His measurements show that, as N is increased from $N << 1$, the drag increases linearly with N to a value of $C_D \sim 0.5$ at $N = 6$. For $N > 6$, $C_D$ increases more slowly with increased N, and appears to be approaching $C_D \sim 0.8$ asymptotically for $N > 20$. Although at low N there are certainly regions of negative pressure on the front of the body (as there are for $N = 0$), these measurements indicate that they are probably not increasing in strength with increased N. The highest drag possible for a halfbody in these flows is $C_D = 1.0$, for which the entire frontal area must be at freestream stagnation pressure. The velocity measurements indicate that it is unlikely that this condition exists in the flow even at $N > 20$, so $C_D \sim 0.8$ can occur only if there is very little negative pressure on the body. Another indication of the pressure near the body comes from some velocity measurements made in the flow downstream of the body. Due to physical limitations imposed by the experimental apparatus, these could only be made for $0.625 \leq r \leq 1.25$ and for only 2 to 3 body diameters past the stagnation point.* Nevertheless, the results are sufficient to indicate that axial velocities in this region were not greater than freestream, but were, in fact, smaller. Typical results of such measurements are included in figures 14 and 20. On the basis of these drag and velocity measurements, it must be concluded that the static pressure on the body near $r = \frac{1}{2}$ is not large and negative, but is probably close to zero. The stagnation pressure in this region would then be

---

* The measurements in the downstream flow are not, therefore, complete enough to allow calculation of the drag using the downstream wake profile and a momentum balance. Such a calculation would have been difficult in any case, since the flow in this region may vary more or less continuously from the body to the tow tank walls. The velocity near the walls, for example, must be $\tilde{U} > 1.03$ due to the blockage effect of the body in the tank and the presence of the wake near the body.

of order $P_o = \frac{u^2}{2} + p < \frac{1}{2}$ , where $u < 1$ and $p$ is approximately zero or at most slightly negative. It should be noted here that because the upstream flow is being forced away from the axis in order to pass the body, the flow outside the disturbance must be accelerating. Since the current regions are broad and extend well beyond $r = \frac{1}{2}$ , especially at large $x_b$, flow at fairly large radial distances is turned and accelerated. As a result, the regions of accelerated flow and stagnation pressure loss past the body are widespread. There is no large radial gradient in axial velocity or, except possibly very close to the body, in stagnation pressure.

## V. CONCLUSION

Velocities in aligned-fields MHD flow ahead of a semi-infinite Rankine body have been measured over a wide range of N. Centerline flow velocities have been measured to within one-half body diameter of the stagnation point, and velocity profiles across the flow to within about five body diameters. It was found that with increased N, the upstream disturbance tends to become more confined radially within the region directly ahead of the body, and that its length increases as $N^{\frac{1}{2}}$. The flow was found to contain a region of stagnant fluid ahead of the body, and a much longer region over which the transition is made from freestream conditions to conditions near the body. The rate at which the length of the stagnant region increases with N was not determined. However, the region was found to be much shorter in length than is predicted by a thin current layer model. The radial gradients of velocity components, pressures, and current density were found to be considerably smaller than suggested by such a model. The results are consistent with a drag coefficient which increases as N is increased and approaches O(1). In the corresponding flow past the body, the radial velocity and current density go to zero, and there are small radial gradients in the axial velocity and the stagnation pressure.

Although a reasonably complete description of the flow has been obtained using the measurements and the inviscid equations of motion for $N >> 1$ and $Rm << 1$, a different flow may evolve as $N \to \infty$. The limiting flow which develops, as N is greatly increased over the values used here, will depend on how the length of the stagnant region increases in relation to the transition region ahead of it. The interaction parameter may have to be much larger than in these experiments before such a limit is approached.

# REFERENCES

1. Liepmann, H. W., Hoult, D. P., and Ahlstrom, H. G., "Concept, Construction, and Preliminary Use of a Facility for Experimental Studies in Magneto-Fluid Dynamics," Mizellen der Angewandten Mechanick, 175-189, 1960.

2. Yonas, G., "Aligned-Fields, Magneto-Fluid Dynamic Flow Past Bodies," Ph.D. Thesis, California Institute of Technology, 1966.

3. Shercliff,J. A., A Textbook of Magnetohydrodynamics, Pergamon, 1965.

4. Suzuki, B. H., "Magneto-Fluid Dynamic Drag Measurements on Semi-Infinite Bodies in Aligned Fields," Ph.D. Thesis, California Institute of Technology, 1967.

5. Childress, S., "On the Flow of a Conducting Fluid of Small Viscosity," JPL Tech. Rept. No. 32-351, Jan. 1963.

6. Childress, S., "The Effect of a Strong Magnetic Field on Two-Dimensional Flows of a Conducting Fluid," J. Fluid. Mech. 15, 429-441 (1963).

7. Tamada, K., "Flow of a Slightly Conducting Fluid Past a Circular Cylinder with Strong, Aligned Field," Phys. of Fluids 5, 817-823 (1962).

8. Maxworthy, T., "Measurements of Drag and Wake Structure in Magneto-Fluid Dynamic Flow about a Sphere," Heat Transfer and Fluid Mech. Inst., 197-205, 1962.

9. Maxworthy, T., "Experimental Studies in Magneto-Fluid Dynamics: Pressure Distribution Measurements Around a Sphere," J. Fluid Mech. 31, 801-814 (1968).

10. Ahlstrom, H. G., "Experiments on the Upstream Wake in Magneto-Fluid Dynamics," J. Fluid Mech. 15, 205-221 (1963).

11. Sajben, M., "Hot Wire Anemometer in Liquid Mercury," Rev. Sci. Instr. 36, 7, 945-949 (1965).

12. Lumley, J. L., "The Constant Temperature Hot Thermistor Anemometer," ASME Symposium on Measurements in Unsteady Flow, Worcester, Mass., May, 1962.

## REFERENCES (cont'd.)

13. Malcolm, D. G., "Some Aspects of Turbulence Measurement in Liquid Mercury Using Cylindrical Quartz-Insulated Hot-Film Sensors." To be published J. Fluid Mech.

14. Chapman, A. J., Heat Transfer, Macmillan, 1960.

15. Hill, J. C., "The Directional Sensitivity of a Hot-Film Anemometer in Mercury," Ph.D. Thesis, University of Washington, Seattle, 1968.

# APPENDIX

The average uncertainties in the directly measured quantities which apply to all of the data in general were:

magnetic field, $B_o$.................$\pm$ 1%
drive shaft velocity, U...........$\pm$ 3%
mercury temperature, $T_{fluid}$.......$\pm$ .1°C

Magnetic field changes produced temperature changes of up to 20°C due to the heating of the magnet. These would have introduced uncertainties of 1% to 2% in the values of parameters such as N or Pé if the mercury physical properties had been considered constant. Because it was possible to calculate all such parameters using mercury physical properties evaluated at the appropriate temperatures, this effect was not present.

## Estimates for X(Pé)

The use of the parameter, $X(P\acute{e}) \propto \left(\frac{\Delta T}{q(0)} - \frac{\Delta T}{q(P\acute{e})}\right)$, requires that the two measurements necessary to determine each data point be made at the same value of $\Delta T$, and for the same sensor coating conditions. The uncertainty in X(Pé) which could arise due to temperature or coating changes during the course of a run can be estimated from the measurements of fluid temperature and zero velocity sensor output made before and after each run.

There was no measurable temperature change during the course of any run, and usually none during each set of runs at a fixed magnetic field. Therefore, since $\Delta T \sim 50^{\circ}C$, each pair of measurements was made at constant $\Delta T$ to within ± .2%. If $\Delta T$ had changed, $X(P\acute{e})$ would have been calculated using $X(P\acute{e}) \propto \left(\frac{\Delta T_1}{q_1(0)} - \frac{\Delta T_1}{q_2(P\acute{e})}\right)$, as opposed to the correct value which would have been $X(P\acute{e}) \propto \left(\frac{\Delta T_1}{q_1(0)} - \frac{\Delta T_2}{q_2(P\acute{e})}\right)$. By comparing these two expressions, Malcolm (Ref. 13) has shown that the error introduced into $X(P\acute{e})$ by the uncertainty in $\Delta T$ can be up to nearly an order of magnitude greater than that of the latter, depending upon the value of Pé. For these experiments this would correspond to a maximum uncertainty in $X(P\acute{e})$ of ± 2%, as a result of the uncertainty in the temperature measurements.

The sensor output at zero velocity was sensitive to variations in both fluid temperature and coating properties. Measurements made before and after each run showed that it changed by less than ± 1% for runs made at high velocities ($P\acute{e} > .5$), and by ± .1% or less for runs made at low velocities ($P\acute{e} < .5$). Equation (2.4), when written as an expression for the measured quantity $q(0)$,

$$q(0) = \frac{\pi k_f L \, (T_{film} - T_{fluid})}{\frac{1}{Nu(0)} + \frac{1}{2}\frac{k_f}{k_c}\,\ell n\,(r_c/r_{film}) + \frac{1}{2}\frac{k_f}{k_c}\,\ell n\,(r_i/r_c)}$$

shows that $q(0)$ may vary due to changes in $\Delta T$, $\frac{1}{Nu(0)}$, and the velocity-independent coating terms. Since $\Delta T$ was known to be constant to within ± .2%, and since it is known that for cylinders in free convection with constant fluid properties $Nu(0) \propto (\Delta T)^{\frac{1}{4}}$, changes in $q(0)$ were due primarily to the coating terms. The above equation can be re-written:

$$\frac{\pi k_f L \Delta T}{q(0)} = \frac{1}{Nu(0)} + C$$

where C represents the coating terms. The use of $X(P\dot{e}) = \pi k_f L \Delta T \left(\frac{1}{q(0)} - \frac{1}{q(P\dot{e})}\right) = \left(\frac{1}{Nu(0)} - \frac{1}{Nu(P\dot{e})}\right)$ assumes that the value of C is the same for the measurements at $P\dot{e} = 0$ and $P\dot{e} \neq 0$. Although large coating changes occurred when the sensor was passed through the mercury free surface, the output from a stationary sensor after immersion indicated that coating properties were then constant except, on occasion, for a very slow drift (see Sec. 2.4). Comparison of $q(0)$ values obtained before and after each run provides an estimate of the effects of whatever coating changes might have occurred during the course of a run. For high velocity runs the variation in $q(0)$ was less than 2% , $\left(q(0) \sim \left(\frac{\text{sensor}}{\text{output}}\right)^2\right)$ , and a 2% change in $\frac{\pi k_f L \Delta T}{q(0)}$ corresponds to a 4% to 6% change in $X(P\dot{e})$, since $X(P\dot{e})$ is 30% to 50% of $\frac{\pi k_f L \Delta T}{q(0)}$. At low velocities both the changes in $\frac{\pi k_f L \Delta T}{q(0)}$ and the values of $X(P\dot{e})$ were smaller by an order of magnitude so that the percentage variation in $X(P\dot{e})$ is again 6% or less.

Estimated in this way, the average uncertainty in

X(Pé) due to temperature and coating effects is something less than ± 6%. However, the most meaningful indication of the average uncertainty in the parameter X(Pé) is that provided by the scatter in the calibration curve. This is of the order of ± 5%.

## Estimates for Pé and u

In the low velocity range where X(Pé) < 0.7, an uncertainty of ± 5% in the value of X(Pé) calculated from the measurements, corresponds to an uncertainty of ± 7% in the value of Pé found using the calibration curve. At higher velocities where X(Pé) becomes a progressively weaker function of Pé, the same uncertainty in X(Pé) corresponds to variations in Pé which increase to the order of ± 15 to ± 20% as X(Pé) → 1.4.

Values of the Pé from the calibration curves were used to calculate the normalized velocities. Although the latter were determined using two different expressions, according to the way in which the data were obtained (see Sec. 2.4), both expressions involved only the values of Pé corresponding to the measured flow velocity, the drive shaft velocity, and the velocity of the displacement flow. The velocity profile of the displacement flow could have become peaked near the axis of the tow tank if the mercury had been permitted to rise through the fringing magnetic field near the top of the tank. For this reason these experiments were performed with the mercury level 7 to 8" below the top of the tow tank. When the sensor was mounted on the tow tank, its output, before the arrival of the velocity disturbance ahead of the approaching body, provided a measure of the displacement flow velocity in the presence of the magnetic field. The displacement velocity measured in this way agreed with that calculated using the drive shaft velocity to within ± 10%. Therefore, to within the accuracy of these measurements, it can be concluded that the magnetic field had no significant effect on the displacement velocity profile.

When the sensor was mounted on the tow tank, the measured values of Pé were in the range $0.03 < Pé < 0.4$. The average uncertainty in the normalized velocity, u, as calculated from equation (2.6), is, therefore, ± 8% due to the estimated uncertainties in $Pé_{meas.}$ and $Pé_{drive\ shaft}$, assuming $Pé_{meas.} >> Pé_{displ.\ flow}$ . The uncertainty in u increases as $u \to 0$, where $Pé_{meas.} \to Pé_{displ.\ flow}$. At $u \sim 0.03$, where $Pé_{meas.} \sim 2\ Pé_{displ.\ flow}$, it becomes ± 20%, and at $u \sim .01$ it reaches ± 40%.

When the sensor was mounted on the drive shaft, the measured values of Pé were in the range $0 < Pé_{meas.} < 2.0$. Equation (2.7) was used to calculate the normalized velocity from these data, so that $Pé_{meas.} = 0$ corresponds to $u = 1$ and $Pé_{meas.} = Pé_{drive\ shaft} - Pé_{displ.\ flow}$ to $u = 0$. Whenever u was greater than or equal to the value of $Pé_{meas.}$ from which it was determined, the uncertainty in u due to that in $Pé_{meas.}$ was no greater than the latter. On the other hand, values of $Pé_{meas.}$ for which $u < Pé_{meas.}$ resulted in values of u which had, as a result of the normalization, a percentage uncertainty increased over that of $Pé_{meas.}$. For $u << Pé_{meas.}$ and high $Pé_{meas.}$ (having the most uncertainty), the possible error in u becomes unacceptably great - even much larger than u itself. In the experiments this situation corresponded to measurements made at high velocities and only moderate magnetic fields, with the sensor drive shaft mounted far enough ahead of the body to be measuring, essentially, the high "freestream" velocity of the flow. It was possible, however, to make measurements for conditions which were equivalent in terms of u vs. $x_b/N^{\frac{1}{2}}$ without having $u << Pé_{meas.}$. This was done, using the sensor mounted in much the same way, by operating at much lower drive shaft velocities and magnetic fields. The data obtained in this way for low u were good to at least ± 15%, except for a few points which are marked with error flags and for which the estimate is ± 20% to ± 40%.

## Estimates for $x_b$

For runs with the sensor mounted on the drive shaft it was possible to measure $x_b$, the sensor-to-body distance, to within ± .015, and the range of $x_b$ was from 0.5 to 4.0 (all in body diameters, i.e., inches). Runs with the sensor mounted on the tank produced data over a continuous range, $2 < x_b < 30$. This distance could be calculated to within ± 4%, but its origin was known only to within ± 0.2 body diameters. The resulting estimated average uncertainty in $x_b/N^{\frac{1}{2}}$ is, therefore, ± 5% for the smallest $x_b$ in the first case, and ± 12% for the smallest $x_b$ in the second.

## Systematic Errors

It should be noted that although the preceding estimates can be made regarding the accuracy of the various measurements and calculations, not all of the data points in any region of figure 12 depend on individual measurements or calculations in the same way. The curve in figure 12 is defined by the overlapping of data obtained for both high and low values of flow velocity past the sensor, and for both small $x_b$ and N, and large $x_b$ and N. In addition, equivalent values of N were produced using different combinations of magnetic field and drive shaft velocity, and there is overlap in the data produced using the two different sensor mountings. While the fact that the results shown in figure 12 were obtained under these varied operating conditions has probably contributed to the overall scatter, it also insures that the data were not subject to systematic errors and that the correlation with $N^{\frac{1}{2}}$ is valid.

## Estimates for Sensor Positioned Off Centerline

The sensor, when not on the axis of the flow in the tow tank, was subject to both an axial component of velocity, u, and a radial component, v. It was decided to use a single sensor and to interpret the measured heat transfer from it as an indication of the axial component of the flow velocity for several reasons. Hot-film sensors have been found to be insensitive to even moderate, ($30^{\circ}$ to $40^{\circ}$), variations of the flow yaw angle in these low Re mercury flows (see Ref. 15). This is due to their relatively low aspect ratio and the thickness and sphericity of the thermal boundary layer. Since the magnetic force tends to suppress radial velocities, it seemed likely that throughout at least the major part of the flow, the direction of the velocity vector would be inclined only slightly with respect to the flow centerline; in other words, that $v \ll u$. As a result, the use of two crossed sensors to provide measurements of both u and v at a point, offers little prospect of success in this kind of flow. The use of crossed sensors would only further increase the sphericity of the thermal boundary layer about each sensor, and further reduce the directional sensitivity of each. In addition, the operational difficulties encountered with the use of one hot-film sensor in mercury could easily become so serious with two sensors that they alone might make accurate measurements virtually impossible. It was, therefore, decided that measurements off the flow centerline would be made using a single tank-mounted sensor.

Measurements were made with the sensor axis both parallel and perpendicular to the radius of the tow tank. Comparison of such measurements provides an estimate of the heat transfer due to the radial velocity, since in one orientation the contribution of the radial velocity is a minimum and in the other it is a maximum. Although the result was usually slightly greater when the sensor was perpendicular to the tank radius, the difference between the results produced in these two ways was never more than the overall scatter in the data. For this reason, and because the flow field indicated by the measurements does not contradict the assumption that $v << u$, the use of the single sensor appears justified.

All of the uncertainties associated with the measurements made with the sensor tank-mounted on the flow centerline apply to the measurements made off of the centerline. When combined and cross-plotted to form velocity profiles at fixed axial positions, these data were subjected to additional scatter due to the fact that not all the runs used in each set of profiles were made at the same value of N. The profiles are made up of data from runs which have values of N within ± 6% of that indicated for the profile. In some cases the scatter in the profiles is as large as ± 25% for the smallest values of $x_b$; i.e., nearest the body. This can be accounted for by the combined effects of the uncertainty in each of the many measurements involved and the amount of data reduction and plotting required to obtain such profiles. Scatter is especially likely near the body where small variations in $x_b$ correspond to fairly large variations in u.

Because $\frac{\partial u}{\partial x} < u$, the uncertainty in the measurements of u is magnified when $\frac{\partial u}{\partial x}$ is used to calculate v. For the lowest N shown in figure 19, the uncertainty in v is a factor of three greater than that in u. For N = 29 this increases to a factor of four to six, depending upon $x_b$. For higher values of N it would have been higher still, so that an uncertainty in u of ± 10% could have produced ± 100% or more uncertainty in v, if such data had been used.

The data used to form the axial velocity profiles were obtained during a series of experiments performed at different times. The operating procedure for the experiments was varied in order to eliminate the possibility of systematic errors. During some operations enough data were taken across the flow at a fixed N to define the velocity profiles for that N. During other operations data were taken at several positions for the whole range of N. Data were obtained using the two sensor radial orientations already described, and the sequence of radial locations at which measurements were made followed no fixed pattern.

Finally, the resulting data were checked against the continuity equation in the following way. The data were plotted in terms of $Pé_{meas.}$ (not the normalized values), to produce profiles of $\dot{P}e_{meas.}$ vs. r at $x_b$. When expressed in this form, the velocity is simply that relative to the tow tank, and the volume flow indicated by the profiles could be compared to that of the known displacement flow at the top of the tank. The volume flow under a profile was calculated by approximating it as a stack of five or six frustrums of cones and summing the volumes of each (in "units" of $\dot{P}e - d^2$). To do this it was necessary to extend the indicated profile shape to $\dot{P}e = 0$ at the base. The results of these calculations for various values of N ranged from 70% to 80% of the volume flow in the displacement velocity at the top of the tank. The profiles would have to be only slightly broader at the base to account for this difference.

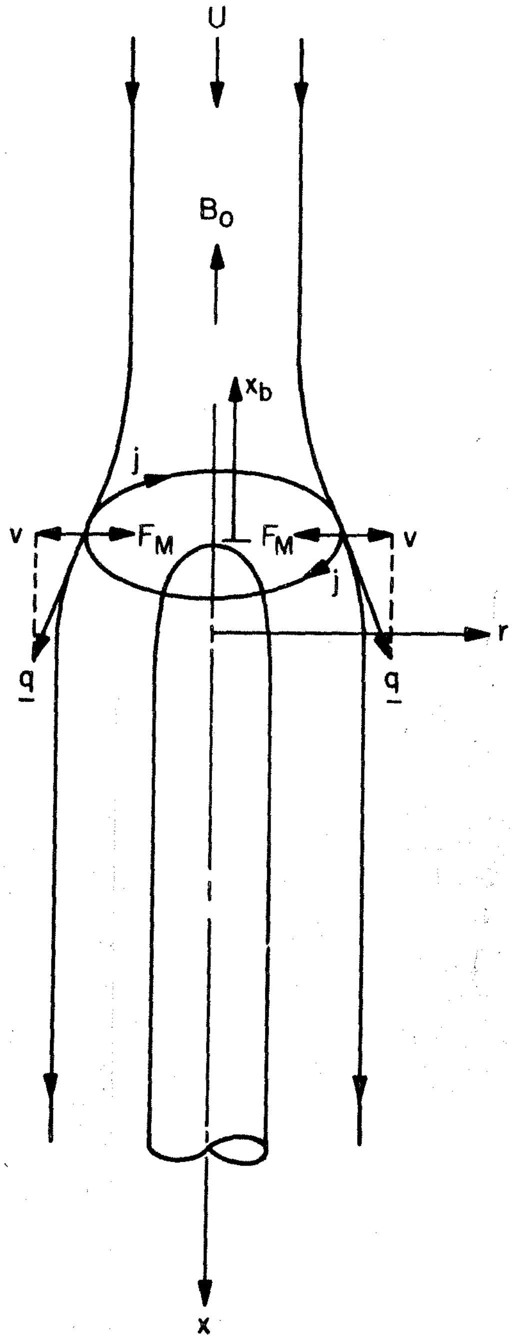

Figure 1. Currents and magnetic forces in axisymmetric MHD flow in the limit Rm → 0.

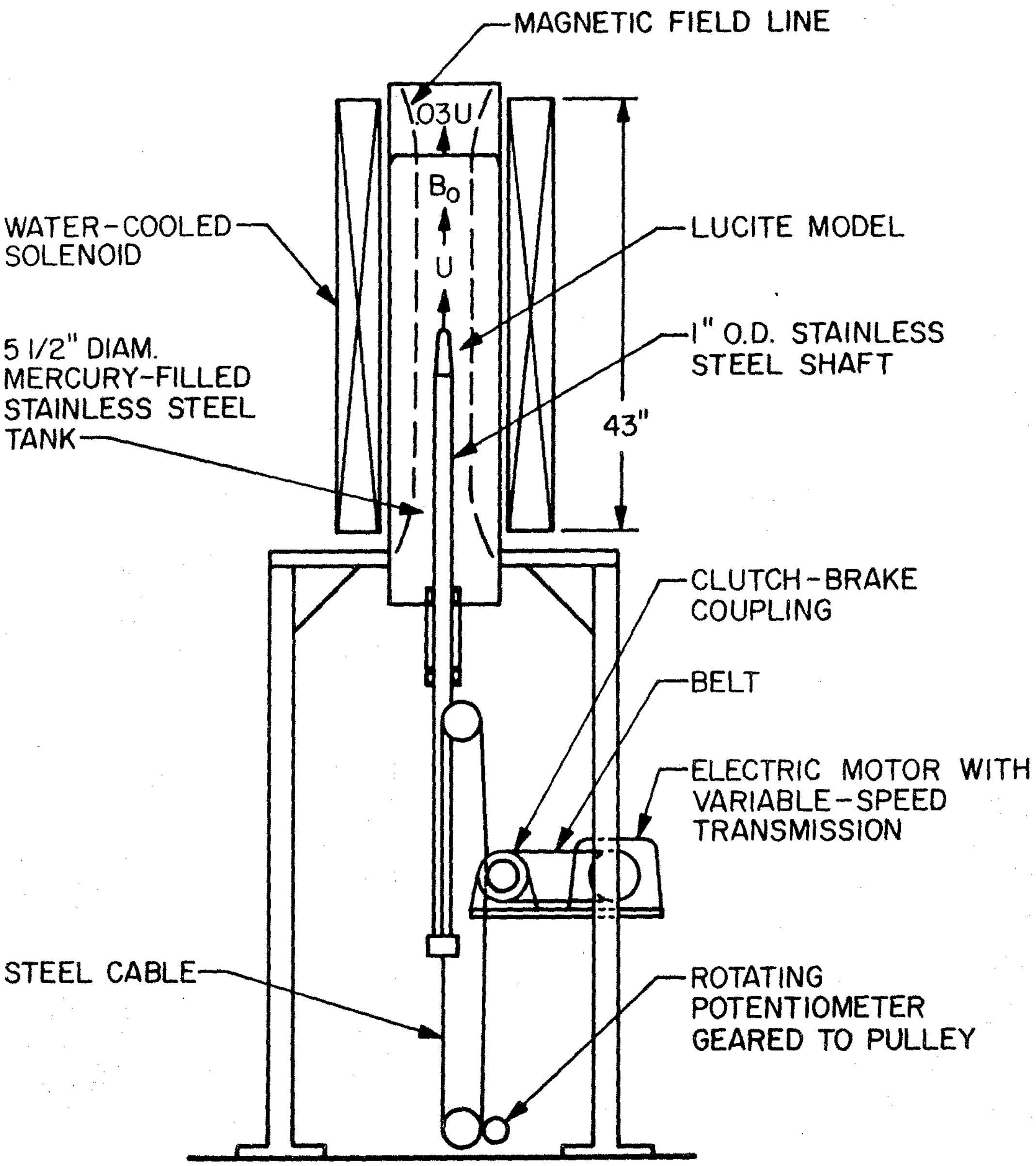

Figure 2. Schematic diagram of the mercury tow tank.

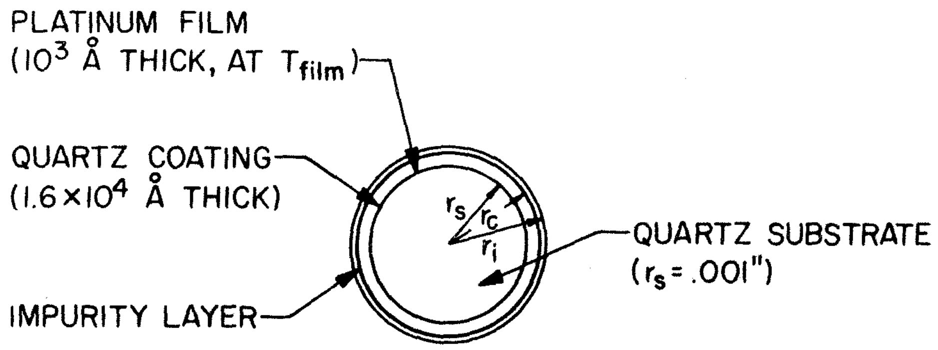

SENSOR CROSS SECTION

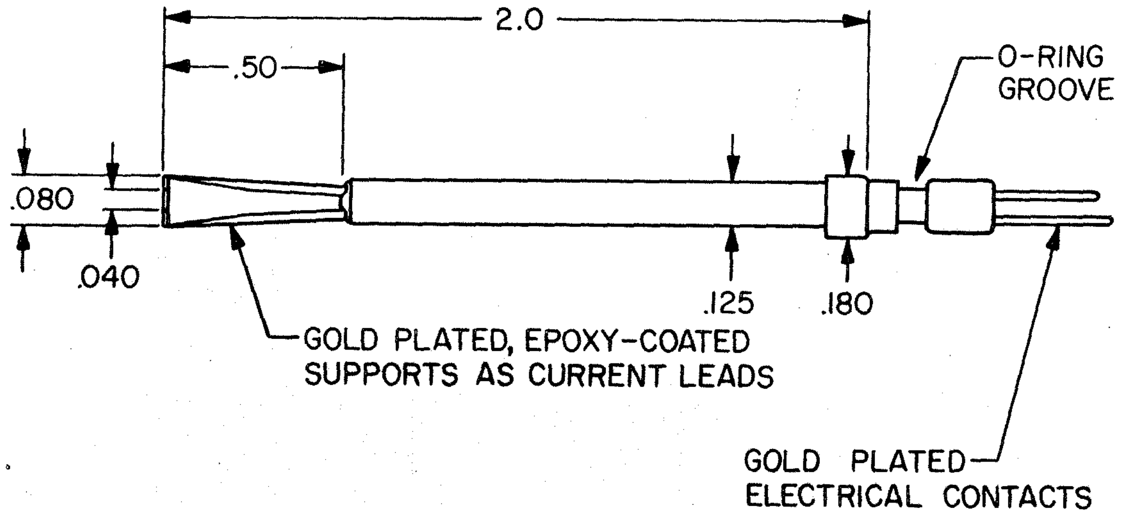

Figure 3. The hot-film sensor.

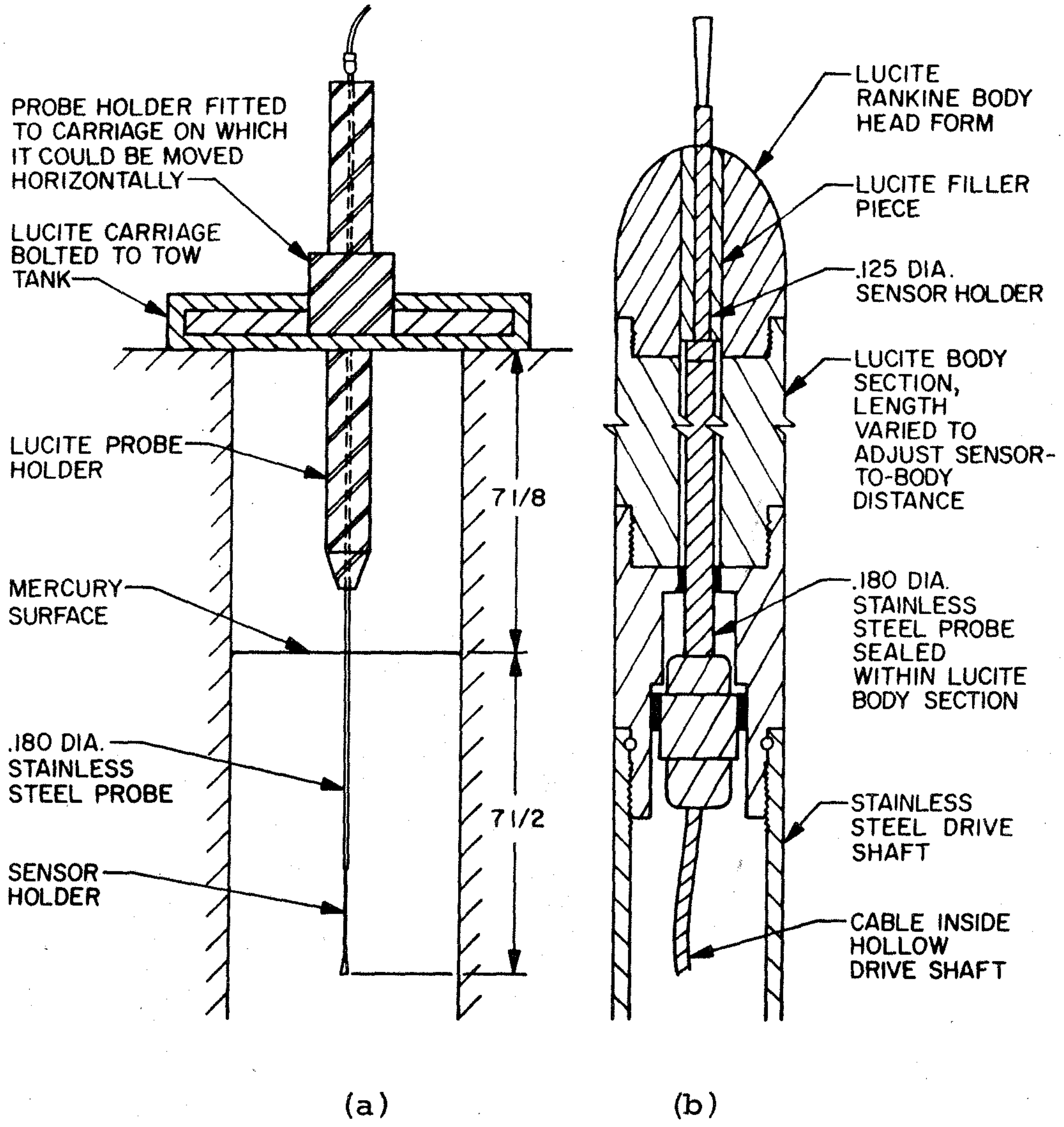

(a) (b)

Figure 4. Sensor mounting positions in the tow tank: (a) tank-mounted, (b) shaft-mounted.

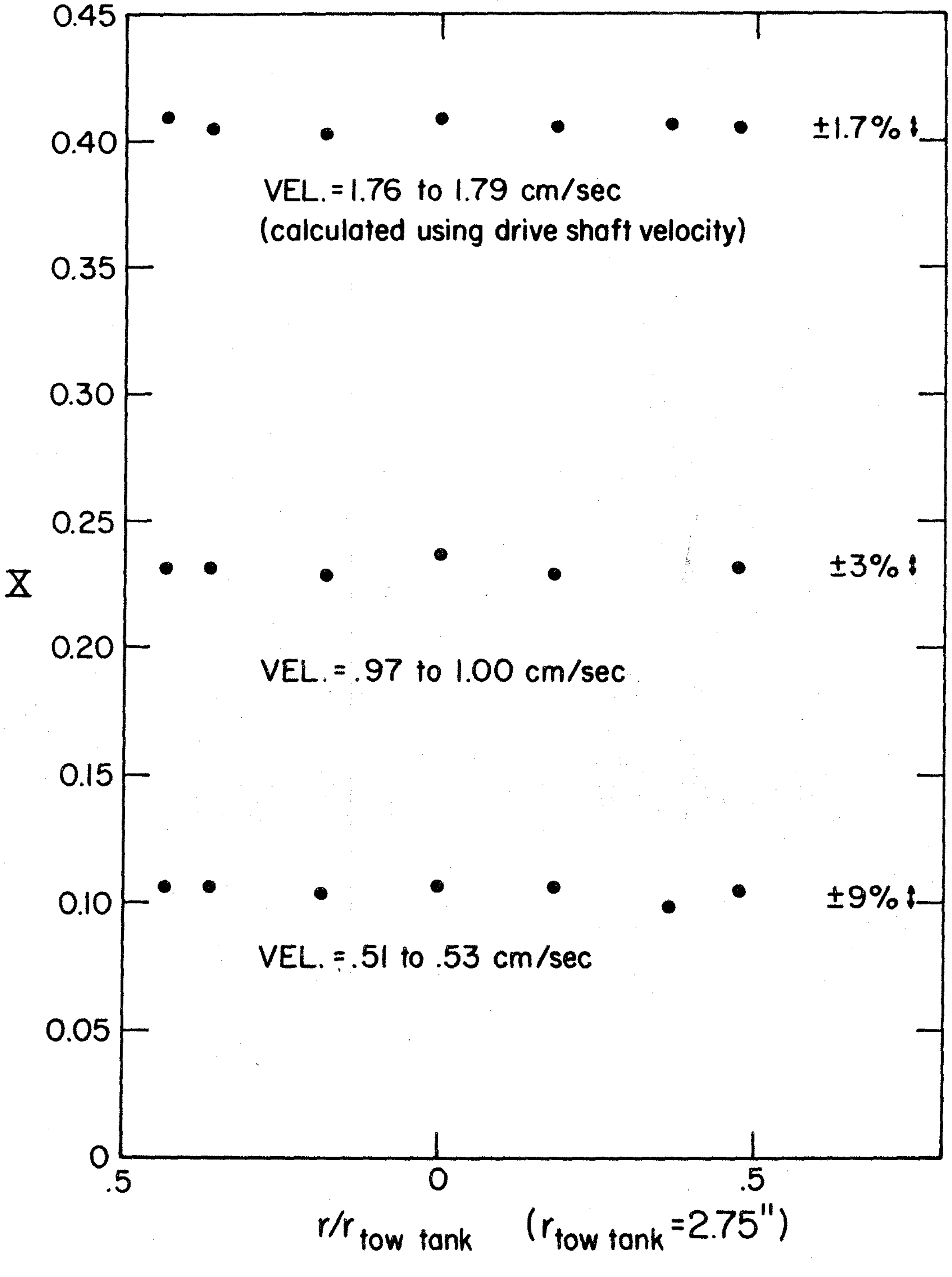

Figure 5. Displacement velocity profiles for N = 0.

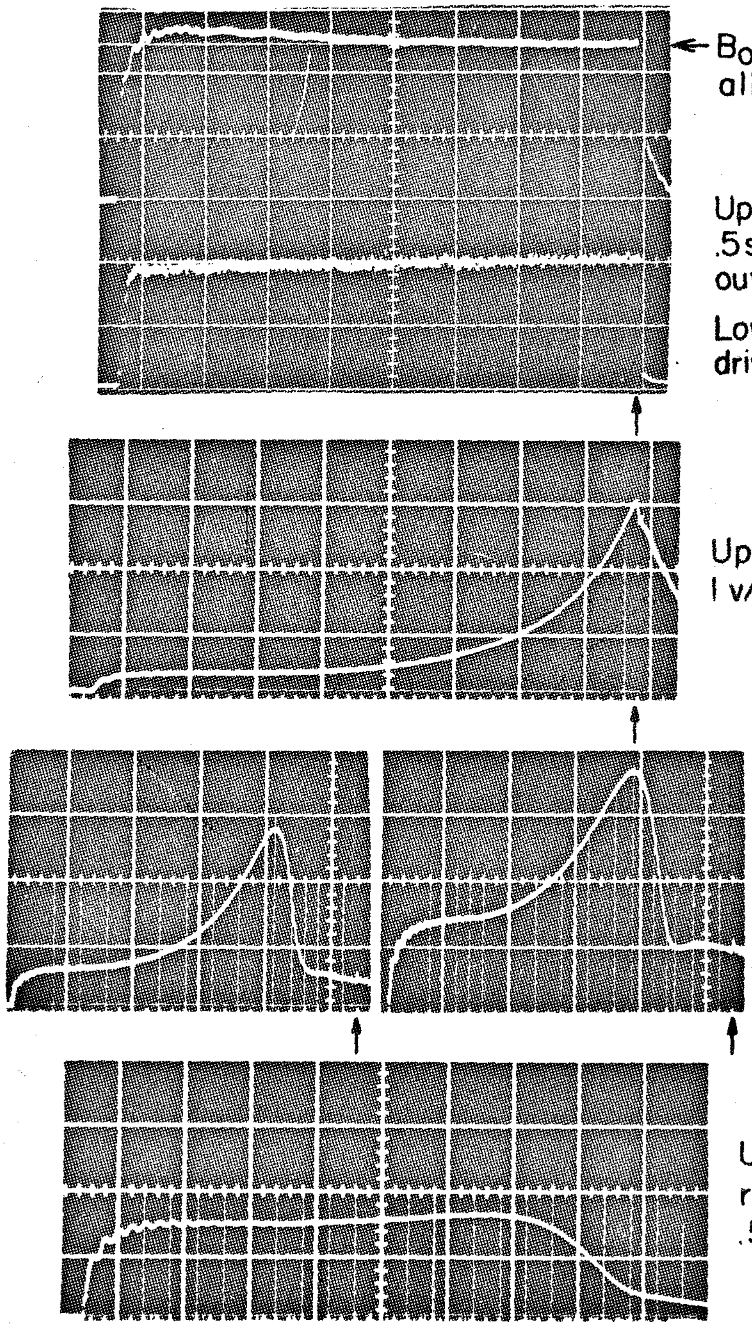

$B_0 = 0$ oscillogram, all others $B_0 \simeq 11{,}300$g

Upper trace: 100mv/div, .5 sec/div, anemometer output

Lower trace: 100mv/div, drive shaft servo output

Upper trace for r = 0, 1 v/div, .5 sec/div

Left: upper trace for r = 5/8, 500 mv/div, 1 sec/div

Right: upper trace for r = 7/8, 200 mv/div, 1 sec/div

Upper trace for r = 5/4, 200mv/div, .5 sec/div

All cases: drive shaft velocity ≃ 15 cm/sec

3 lowest cases: body allowed to pass sensor

Time increases left to right, arrows show end of run

Figure 6. Oscillograms for tank-mounted sensor data.

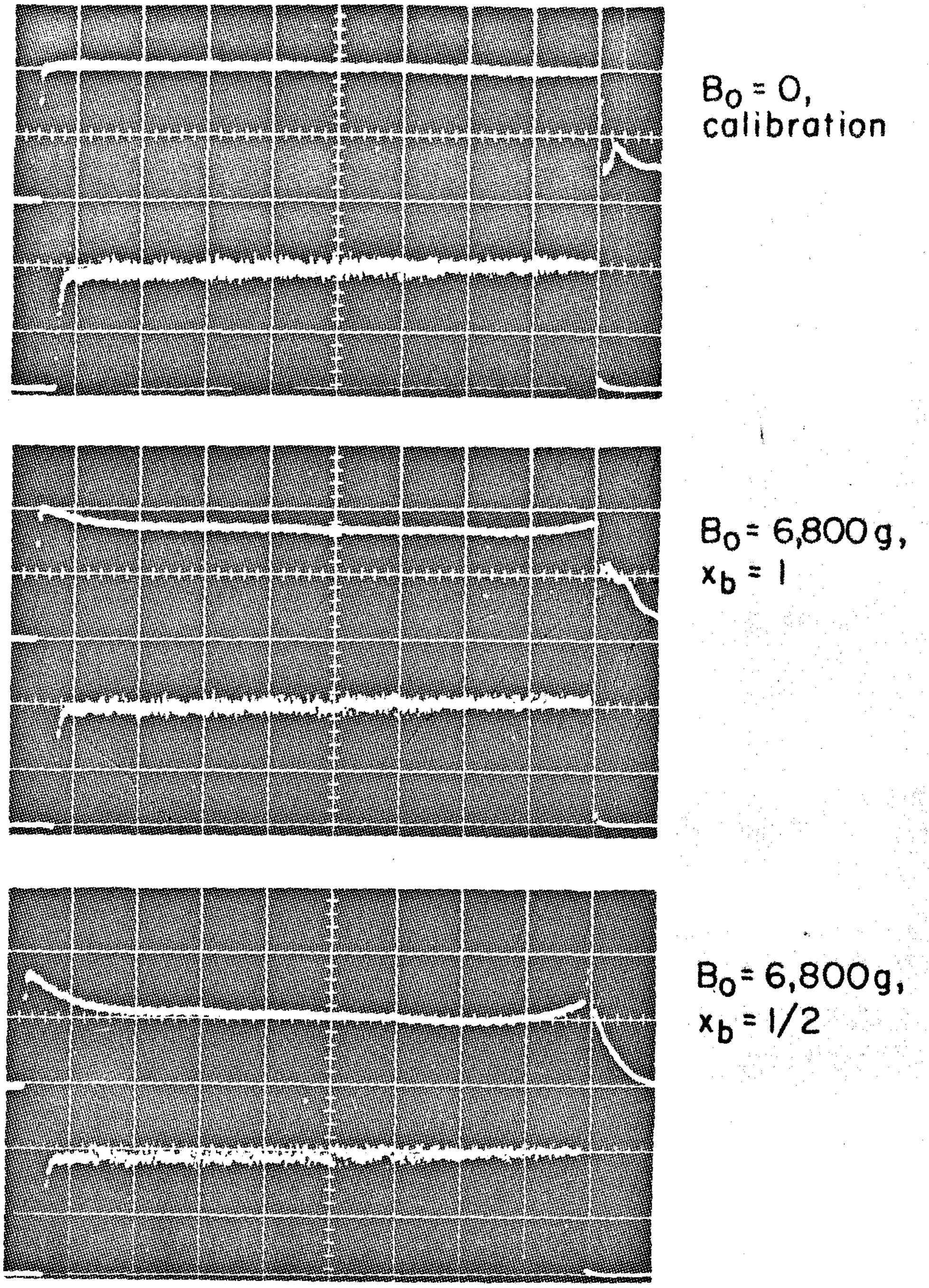

All upper traces: 2 v/div, anemometer output
All lower traces: 100 mv/div, drive shaft servo output
All cases: .5 sec/div, drive shaft velocity ≃ 15 cm/sec

Figure 7. Oscillograms of shaft-mounted sensor data.

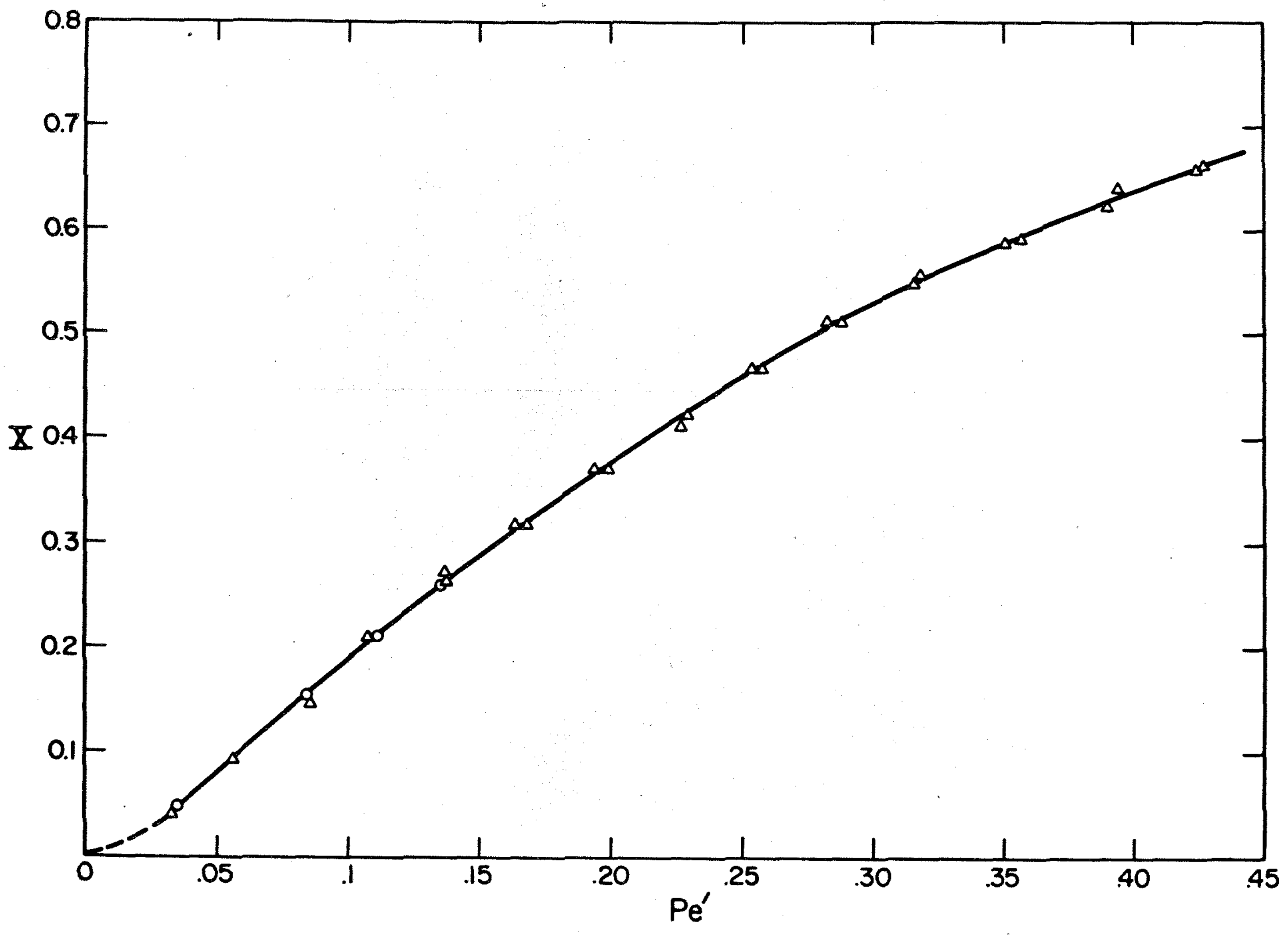

Figure 8. Sensor calibration curve.

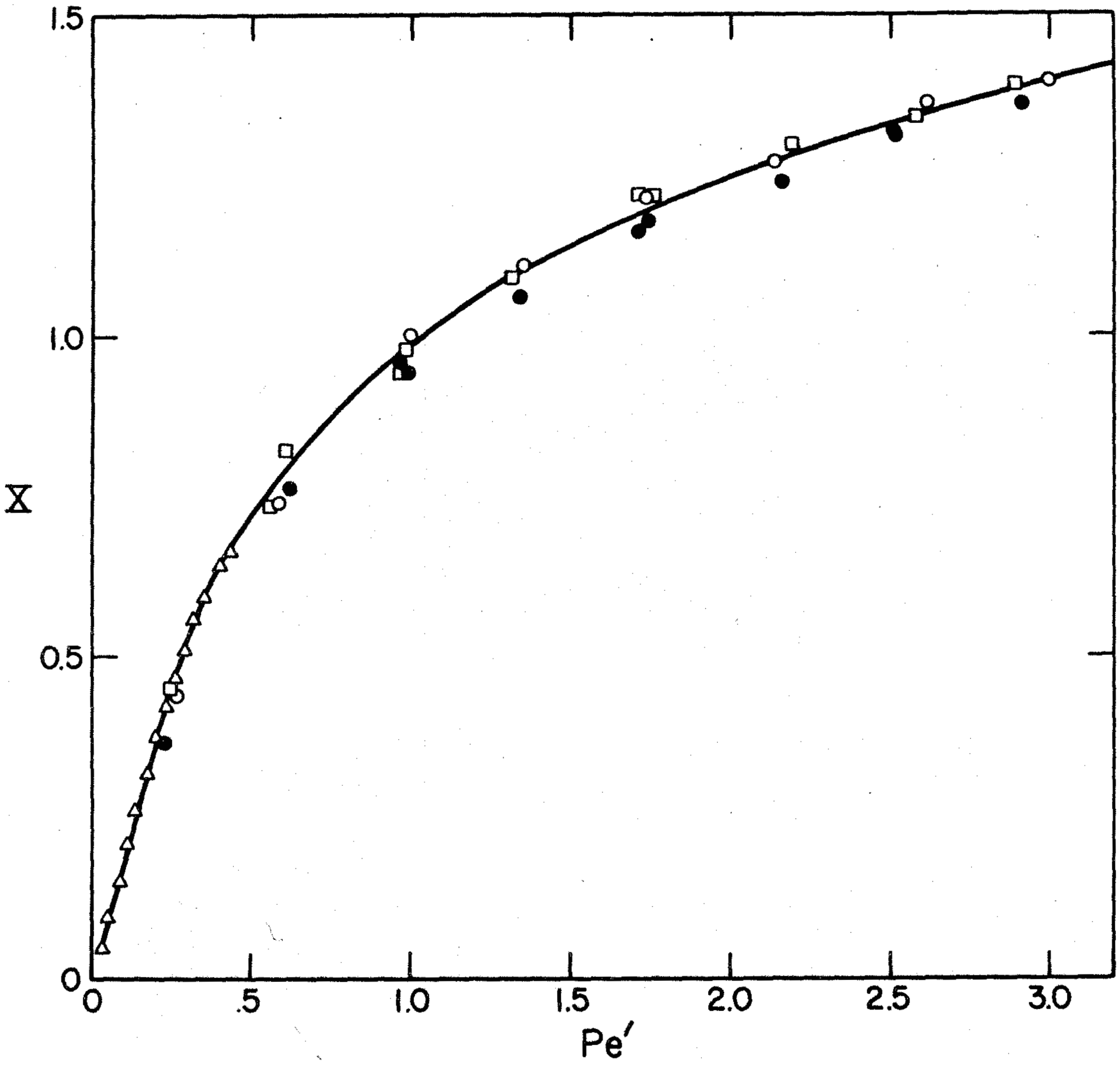

Figure 9. Sensor calibration curve.

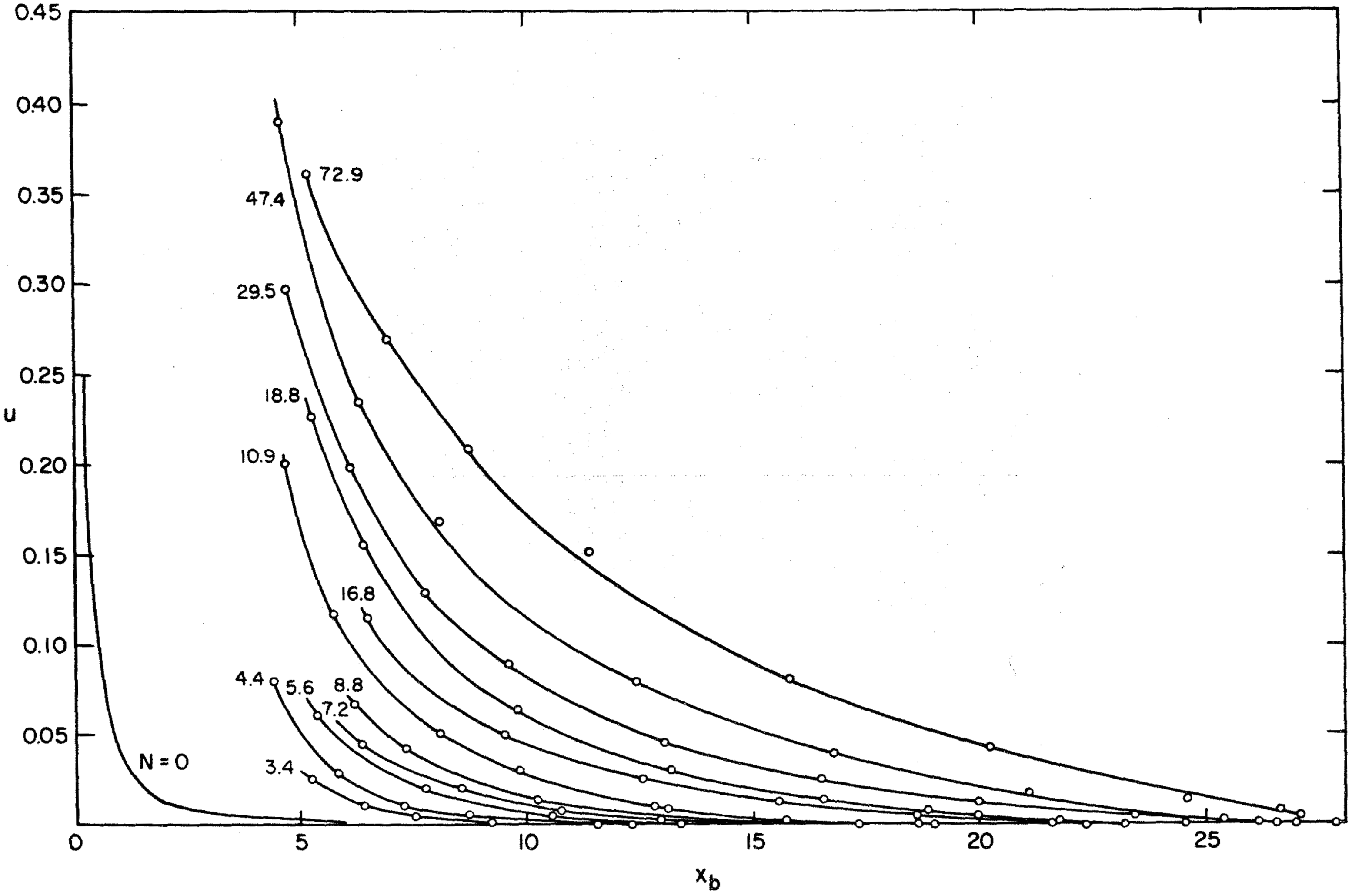

Figure 10. Normalized velocity on the flow centerline vs. distance from body for a range of interaction parameters.

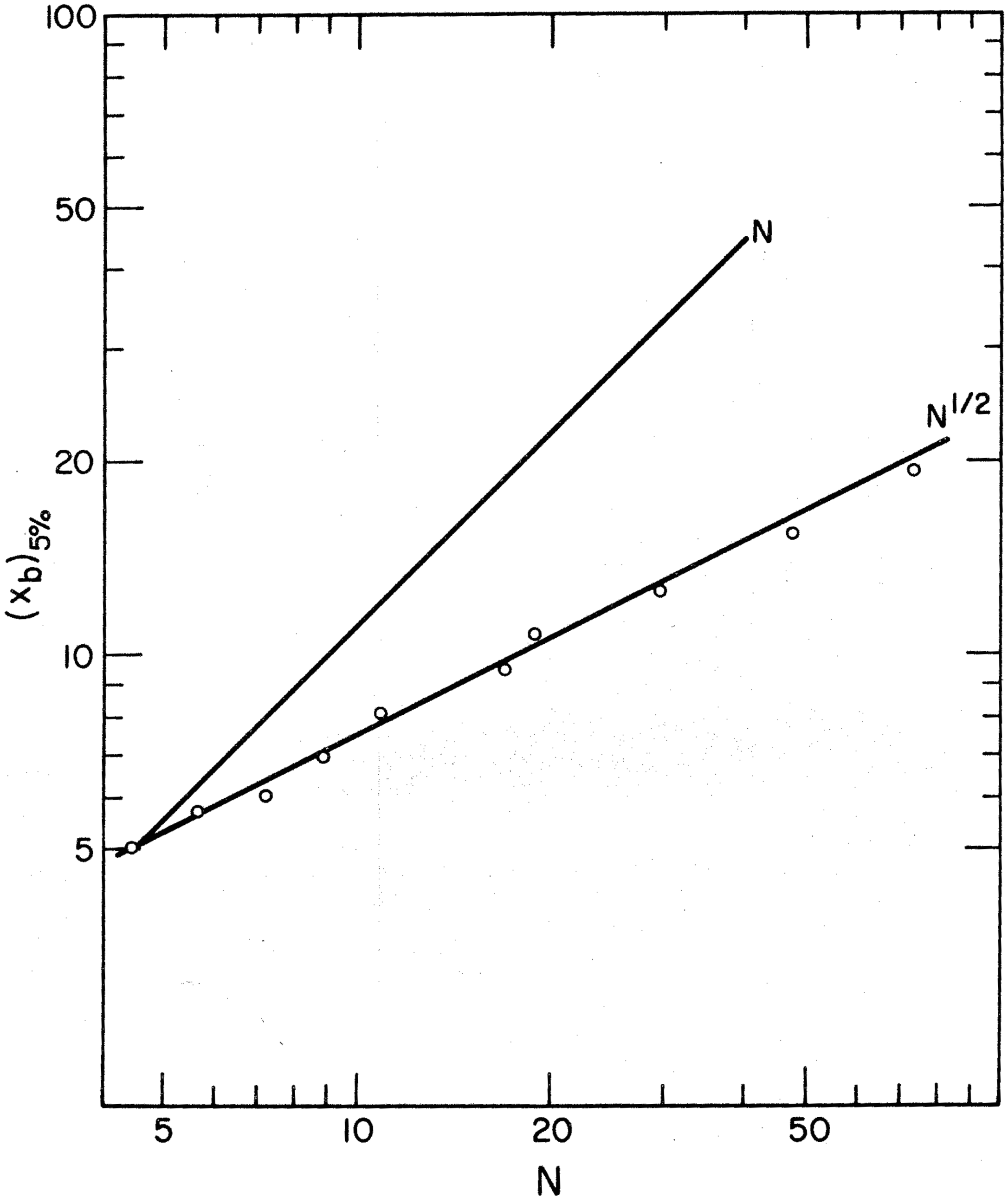

Figure 11. Disturbance length vs. interaction parameter.

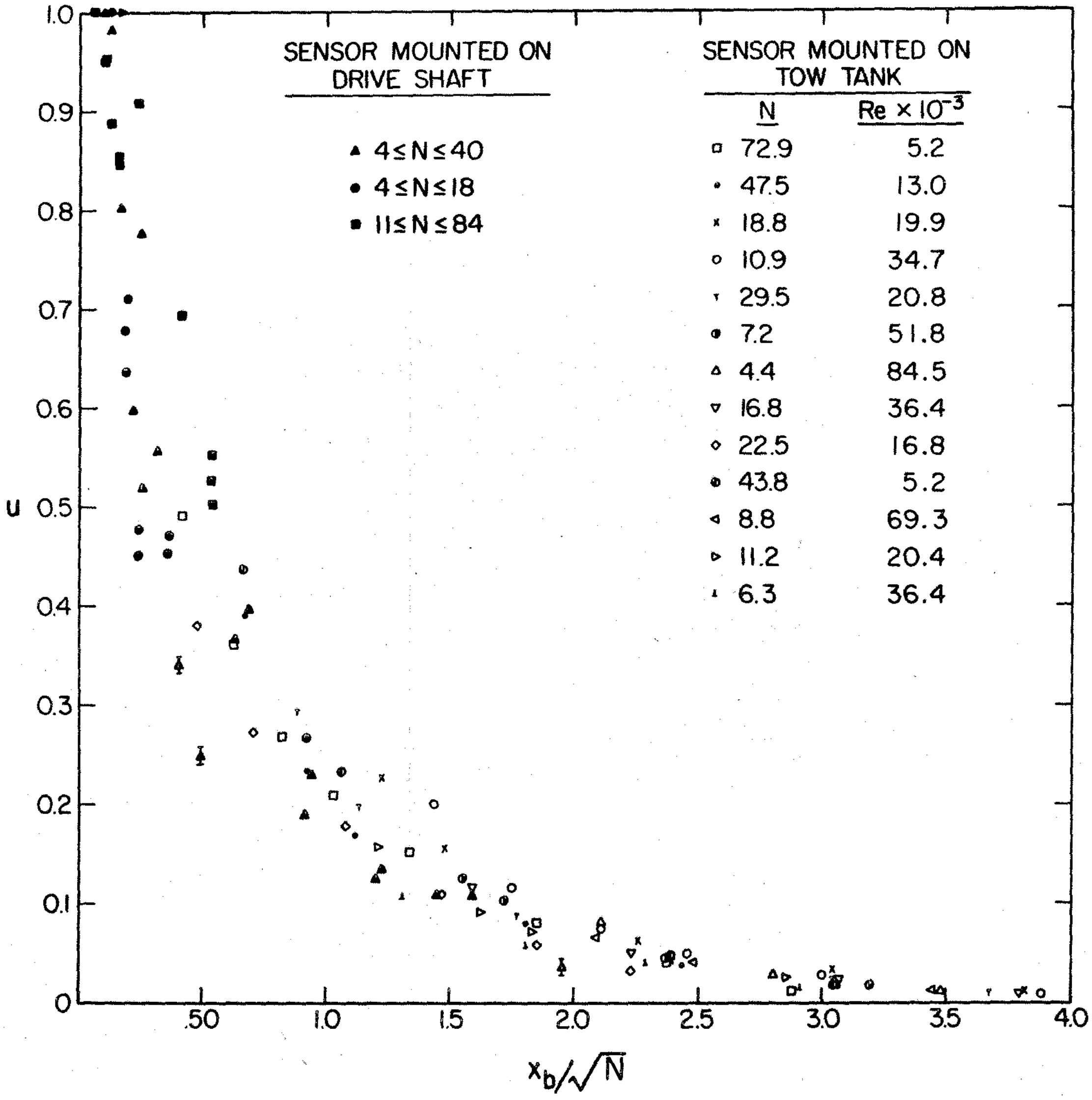

Figure 12. Normalized velocity on the flow centerline vs. $x_b/\sqrt{N}$.

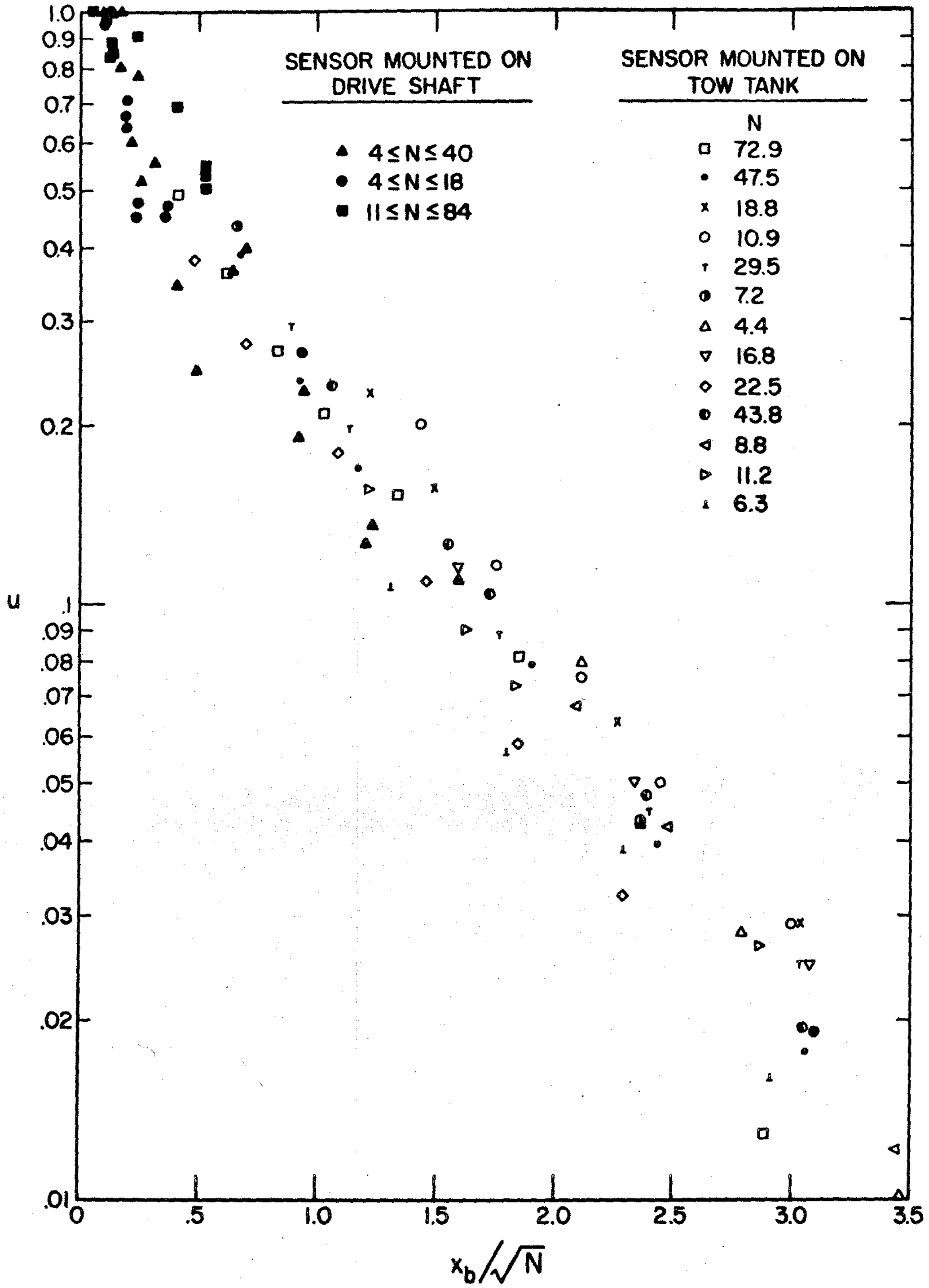

Figure 13. Normalized velocity on the flow centerline vs. $x_b/\sqrt{N}$.

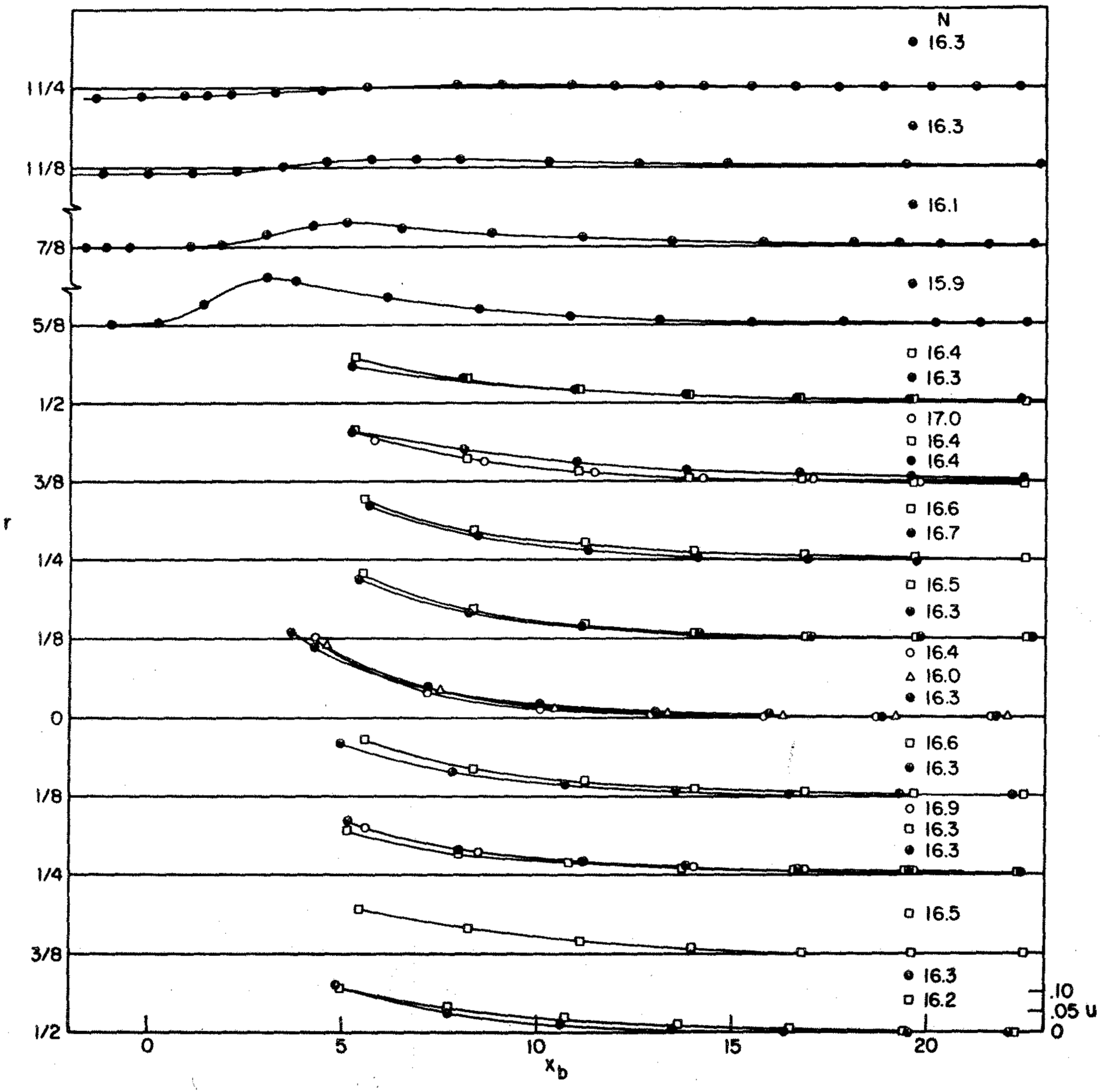

Figure 14. Examples of normalized velocity vs. distance from body measured at various radial positions in the flow.

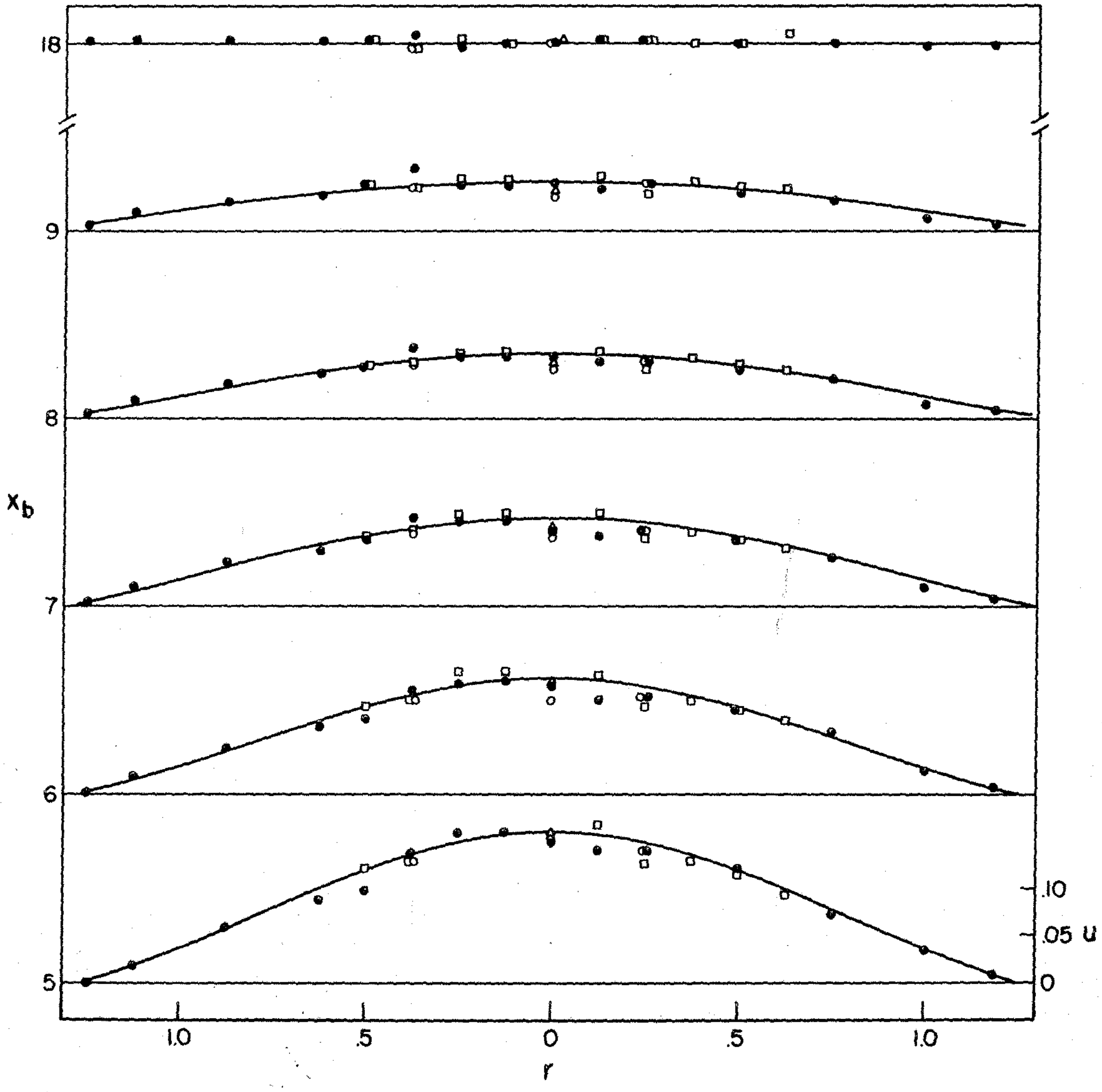

Figure 15. Normalized axial velocity profiles for N = 16.4.

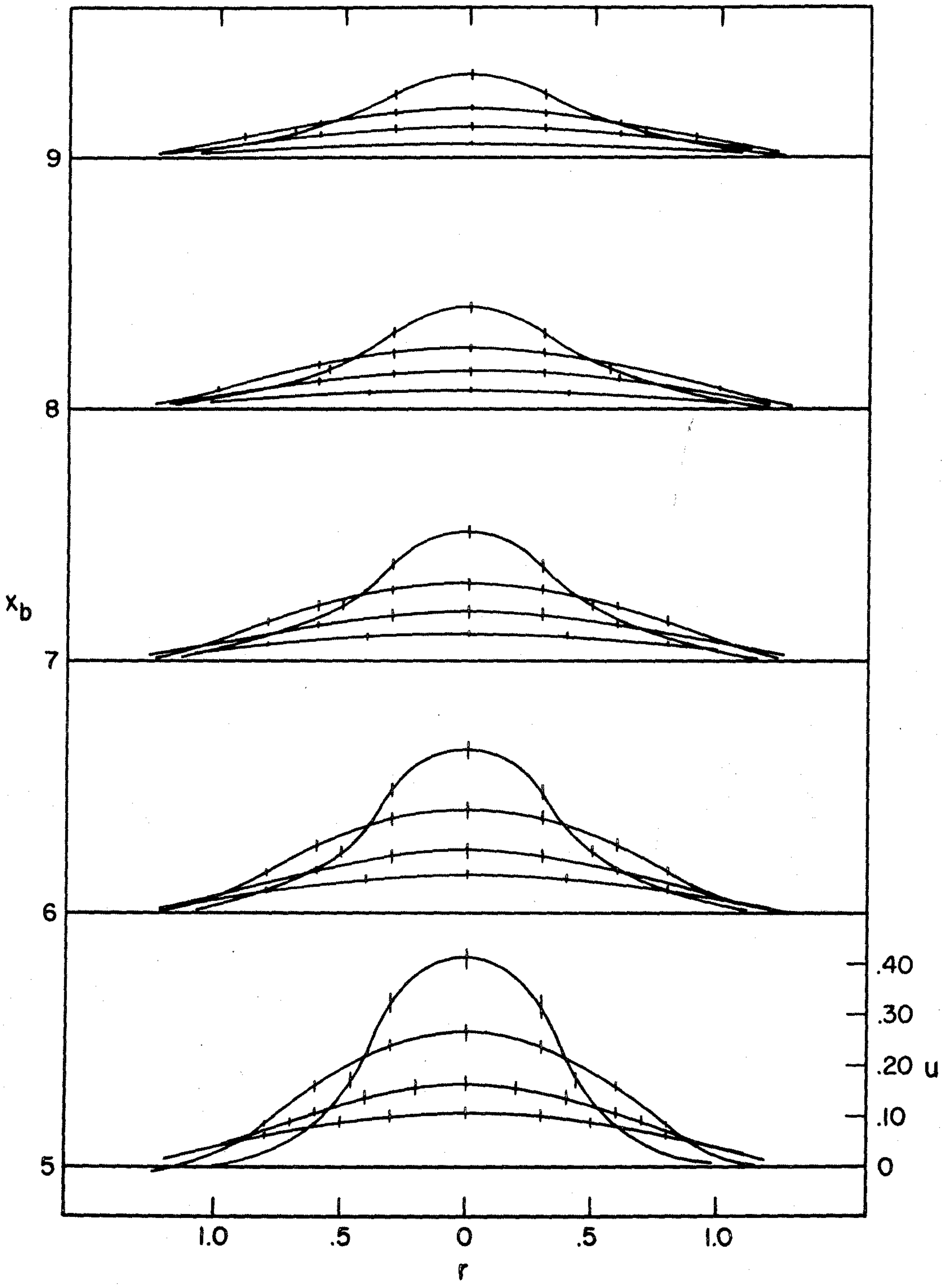

Figure 16. Normalized axial velocity profiles for N = 11.2, 16.4, 29, and 47.

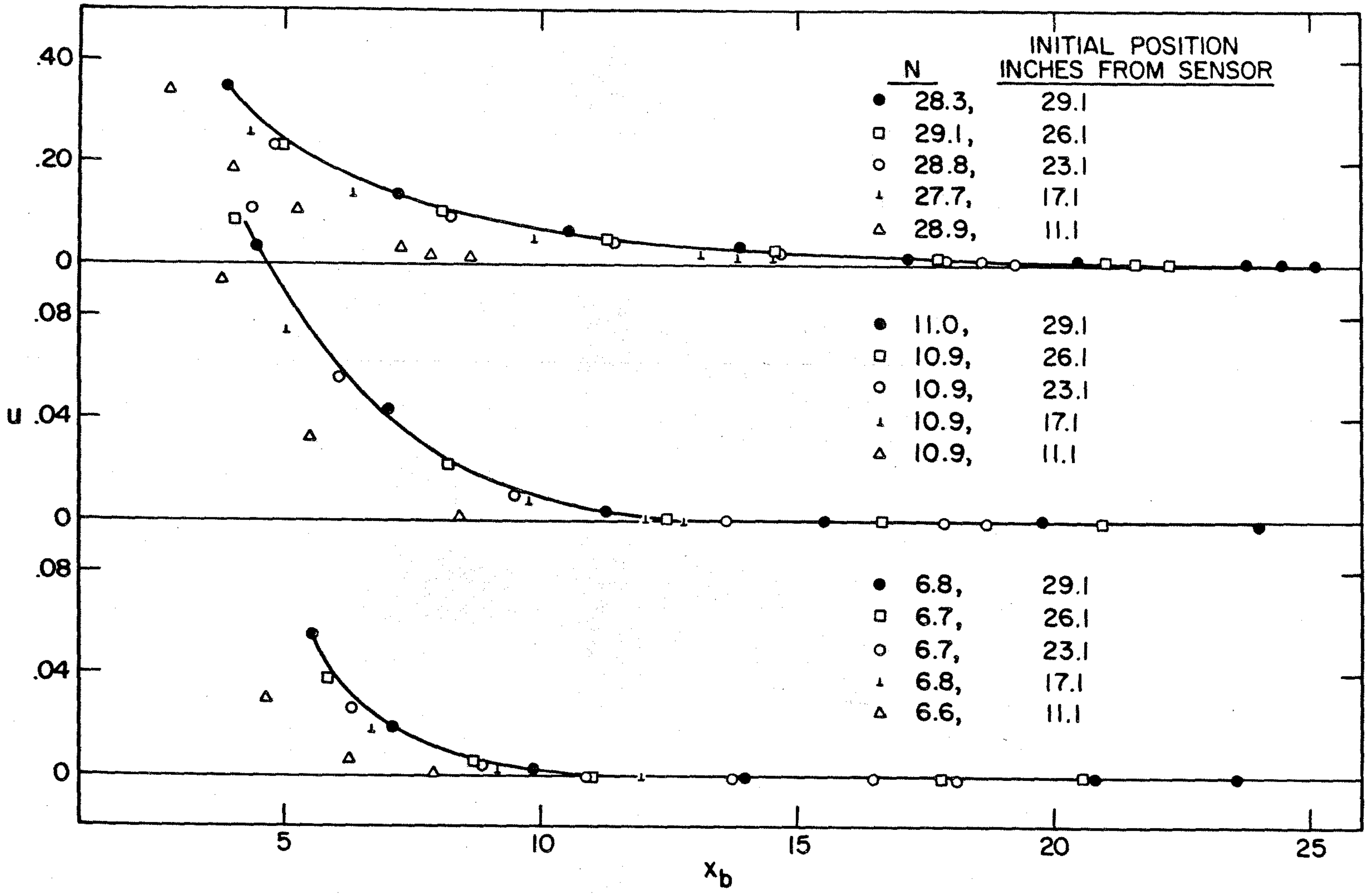

Figure 17. Normalized centerline velocity measurements for a range of drive shaft initial positions.

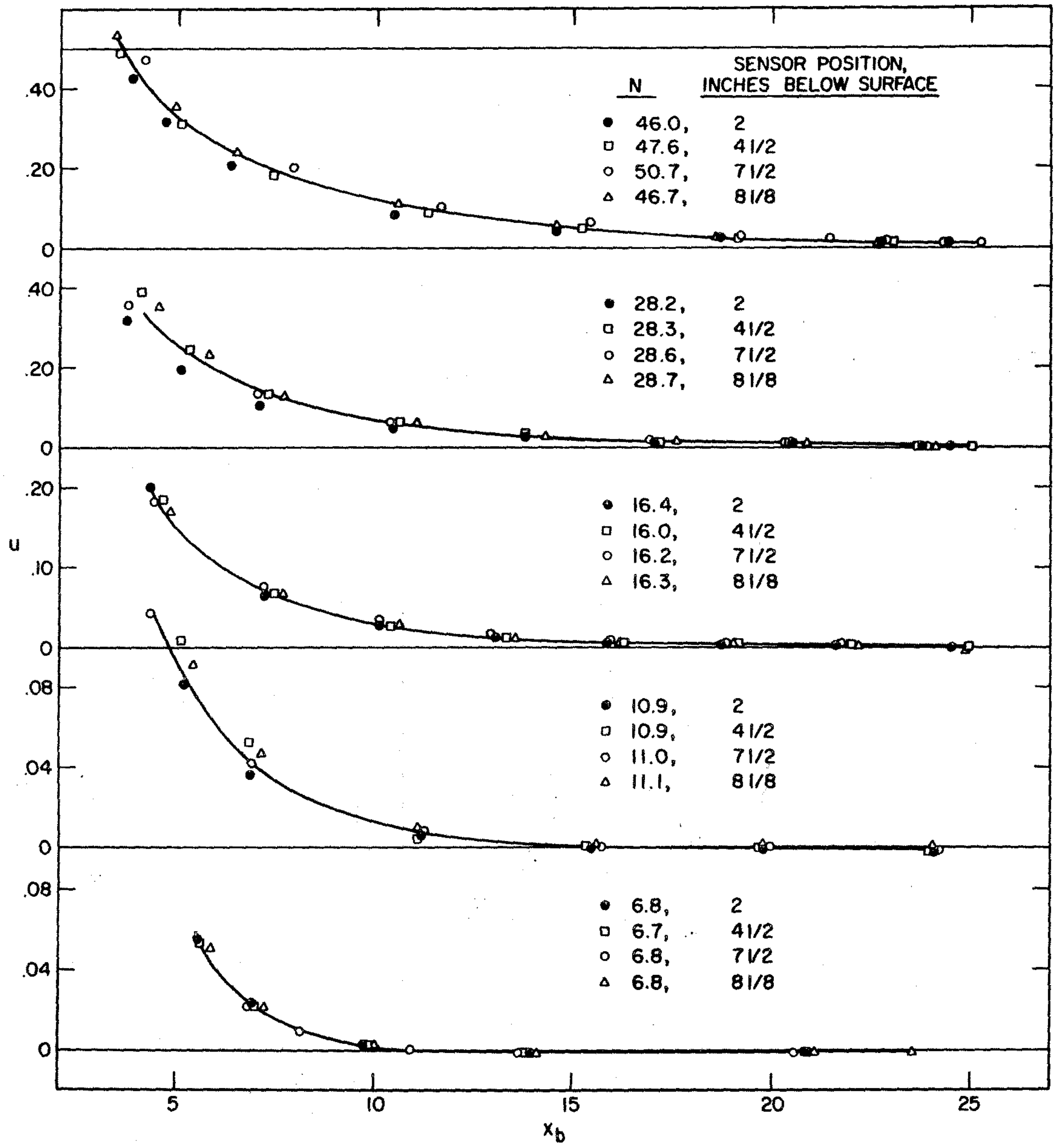

Figure 18. Normalized centerline velocity measurements for a range of mercury surface positions.

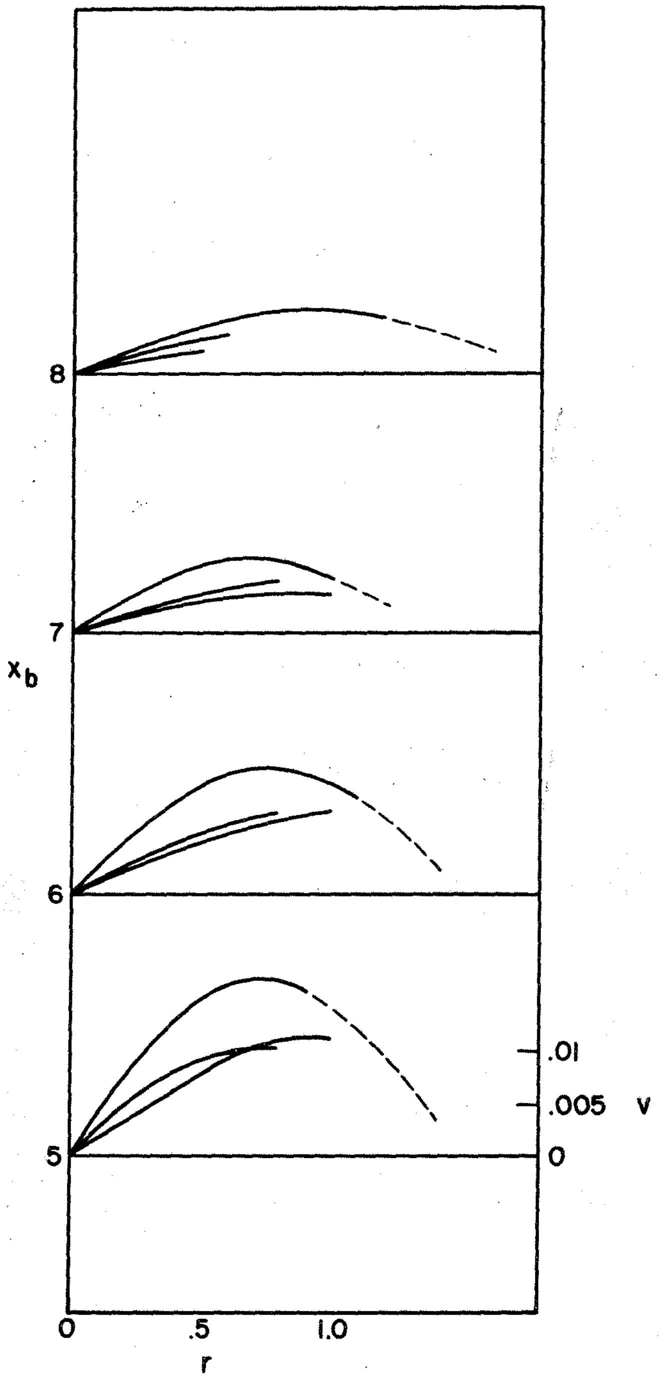

Figure 19. Normalized radial velocity profiles for N = 11.2, 16.4, and 29.

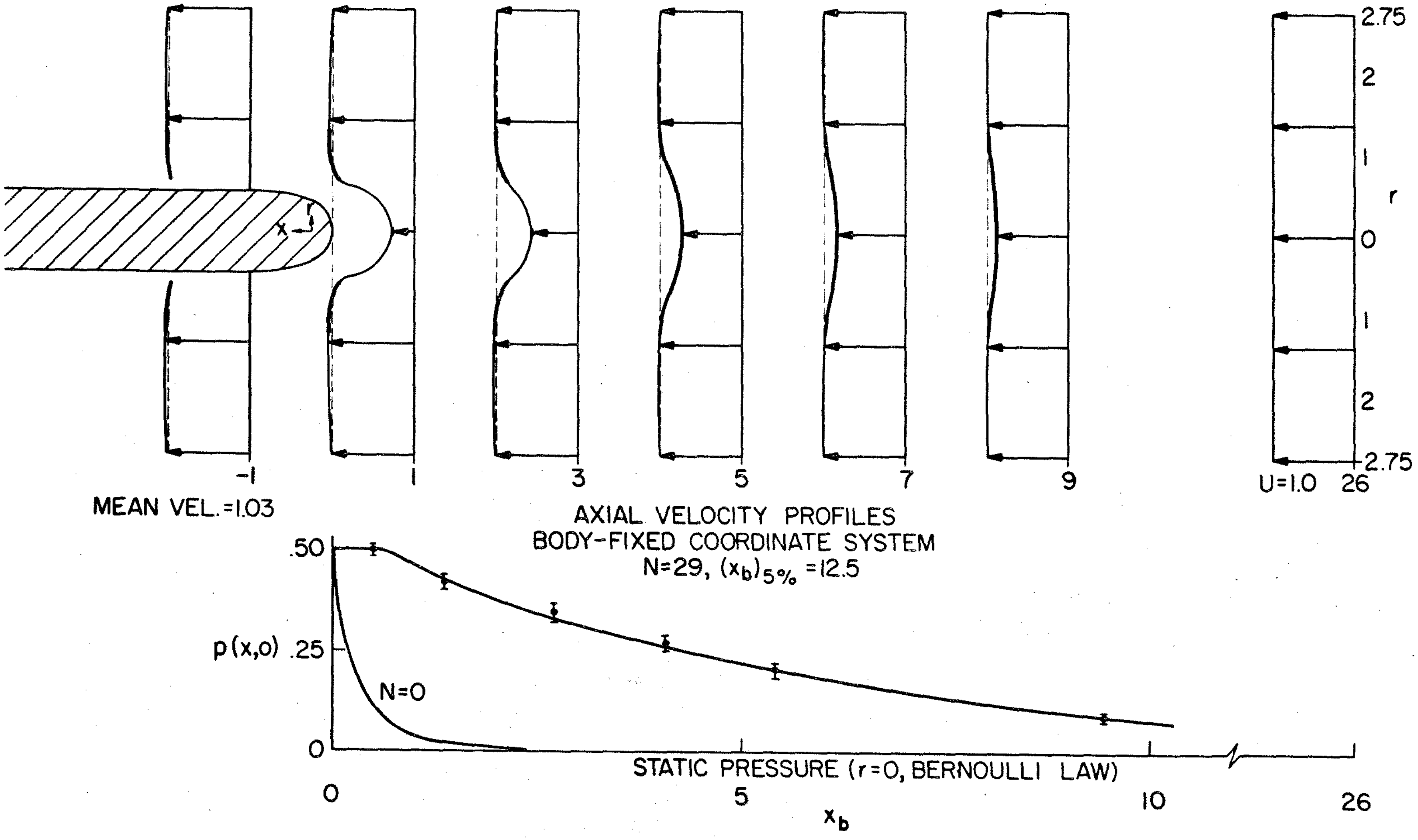

Figure 20. Flow in the tow tank for N = 29.